

Cosmological Simulation with Population III Stellar Feedback and Metal Enrichment I: Model Description And Convergence Test

Bocheng Zhu*

Institute of Astrophysics, School of Physics, Zhengzhou University, China

Liang Gao†

Institute of Astrophysics, School of Physics, Zhengzhou University, China and

*Institute for Frontiers in Astronomy and Astrophysics,
Beijing Normal University, Beijing 102206, China*

(Dated: February 16, 2026)

We present a new Pop III + Pop II subgrid framework implemented in the moving-mesh code AREPO, designed to study the impact of Pop III feedback on star formation in the early universe. The framework combines primordial non-equilibrium chemistry, metal-line cooling, IMF-sampled stellar evolution with SN feedback, and approximate Lyman-Werner (LW) and ionizing radiation transport. We run a suite of $1\text{cMpc}/h$ box simulations with different initial conditions and resolutions from $z = 127$ to $z = 10$. The highest gas mass and spatial resolution in the fiducial simulation reach $\sim 10 M_\odot$ and $\sim 4\text{pc}$, respectively. The model successfully reproduces the UV-inferred Pop II star formation rate density (SFRD) from recent JWST observations across all initial conditions, with only minor variation driven by local halo interactions and LW irradiation. We find that the volume filling factor of metal-enriched gas converges to $\sim 1\%$ at $z = 10$. Convergence is achieved once subhalos with $M_{\text{subhalo}} \gtrsim 10^{6.5} M_\odot$ are resolved, and the total stellar mass at $z = 10$ is largely insensitive to initial conditions or the resolution considered in this work. A fiducial simulation requires $\sim 10^4$ CPU hours, making the framework computationally tractable for larger box simulations and enabling future large parameter studies of stellar physics or environment effects such as Pop III IMF variations, X-ray radiation, or the streaming velocity at high redshift.

I. INTRODUCTION

The first generation of stars, known as Population III (hereafter Pop III) stars, plays a key role in shaping the initial thermal, chemical, and radiative conditions of the early Universe [1–3]. Forming from pristine, metal-free gas in minihalos at high redshift, these stars provide the first ionizing photons that contribute to cosmic reionization [4]. Furthermore, through supernova (SN) explosions, Pop III stars enrich the pristine intergalactic medium (IGM) with the first heavy elements, fundamentally altering the cooling properties of the gas and regulating the formation of the subsequent metal-enriched Population II (hereafter Pop II) stars and the first galaxies [5–13]. Understanding how Pop III stars form and impact their environment in the early universe is therefore essential for understanding the cosmic history.

Despite their crucial importance, direct observation of individual Pop III stars remains elusive due to their faintness and extreme distances. One promising avenue is stellar archaeology, i.e., the observation of metal-poor stars in the Milky Way to seek relics of Pop III stars [14, 15]. Massive Pop III stars are predicted to end their lives as gamma-ray bursts [16] or pair-instability supernovae (PISN) [17]. These energetic events enrich the surrounding medium, leaving distinctive fingerprints on the second-generation stars formed from the ejecta [18, 19]

and in the spectra of high-redshift GRBs [20, 21]. Potential PISN signatures have been identified in the Milky Way halo [22, 23], and in nearby dwarfs [24].

Complementary to these local archaeological efforts, the recent launch of the James Webb Space Telescope (JWST) has revolutionized our study of the high-redshift Universe. JWST observations have begun to uncover galaxy candidates at $z \gtrsim 10$ [25–28], with a potential Pop III signature found via lensing [29]. While these observations provide unprecedented constraints, disentangling the signatures of Pop III stars from early Pop II populations is challenging.

On the other hand, indirect constraints from large-scale observables offer a complementary avenue to probe the first stars. Theoretically, the imprint of Pop III stars on the cosmic background has been studied extensively over the past decades. Several works using semi-analytic models [30, 31] and semi-numerical codes [21cmFAST; 32] have established how the UV and X-ray backgrounds from the first stars likely shaped the thermal and ionization history of the IGM. This field has seen a surge of renewed interest recently, driven by the arrival of observational data. New upper limits on the 21-cm power spectrum from experiments like HERA [33] and constraints on the global signal from SARAS 3 [34] have begun to place the first stringent constraints on the Pop III parameter space [35].

To ground these statistical inferences in robust physics, we also need to understand how variations in Pop III star properties affect the environment and how they, in turn, regulate subsequent star formation. This requires

* zhubc@shao.ac.cn

† lgao@bao.ac.cn

a modeling approach that connects micro-scale stellar physics and macro-scale cosmological simulations. However, modeling Pop III stars in cosmological simulations is challenging. Since Pop III stars form from molecular hydrogen (H_2) clouds, capturing this process requires solving the non-equilibrium chemistry of the primordial gas [36–38]. The evolution of Pop III stars is also different from metal-enriched stars in the local universe because of their extremely low metallicity [17, 39, 40]. Furthermore, the initial mass function (IMF) of Pop III stars remains highly uncertain [41–43]. Finally, since Pop III stars form in low-mass minihalos, high resolution to resolve them is required for the cosmological simulations [44, 45].

Over the past decades, extensive efforts have been dedicated to simulating Pop III star formation and feedback within a cosmological context. Pioneering zoom-in simulations focused on the formation of the first stars in individual minihalos [45–48]. To capture the statistical properties of early galaxies, subsequent studies extended these methods to larger volumes. Notable examples include the Renaissance Simulations [9, 49, 50], as well as other campaigns [e.g., 51–53]. More recently, state-of-the-art simulations have incorporated increasingly detailed physical processes such as on-the-fly radiative transfer (RT), non-equilibrium dust evolution and explicit Pop III modeling, to study the epoch of reionization. Related projects in this category include AEOS [12], and MEGATRON [13, 54]. Complementarily, the properties of Pop III stars and their transition to Pop II have been analyzed in high-resolution cosmological zoom simulations [e.g., 55].

These simulations have successfully captured the complex interplay between Pop III star formation, feedback mechanisms, and larger-scale cosmological evolution, providing invaluable insights into how these early stars influence the formation of galaxies. However, despite their remarkable success, these high-resolution cosmological (zoom) simulations are computationally expensive. This high cost limits the feasibility of conducting large parameter space studies, making it challenging to explore how the full range of uncertainties in Pop III models impacts galaxy formation at early epochs.

In this paper, we present a new Pop III + Pop II subgrid framework implemented in the moving-mesh code AREPO [56]. Our model integrates a primordial non-equilibrium chemical network, metal-line cooling, and a stochastic IMF sampling scheme that explicitly accounts for SN feedback. Furthermore, we incorporate an approximate radiative transfer method to model Lyman-Werner (LW) and ionizing radiation feedback efficiently. As the first paper in a series, our primary goal is to establish a robust framework that is computationally tractable, enabling future extensive investigations into how physical uncertainties related to Pop III stars shape the properties of the early Universe and the formation of the first galaxies.

The paper is organized as follows. We describe the models in detail in Section II, including the modeling of star formation, stellar feedback from Pop III and

Pop II stars, non-equilibrium chemistry and gas cooling/heating, metal yields, the refinement strategy, and the simulation setup. In Section III, we introduce the main results, including the time evolution, the star formation history, and the gas properties of the simulations with fiducial resolutions but different initial conditions. In Section IV, we investigate the resolution convergence of our model. Finally, we summarize in Section V.

II. METHODS

In this section, we introduce the subgrid models and numerical implementations for star formation, stellar feedback, non-equilibrium primordial chemistry, and radiative cooling within our Pop III cosmological simulation framework. In Section II A, we describe the star formation criteria for both Pop III and Pop II populations. The stellar feedback models, including supernova feedback from both populations and stellar winds from massive Pop II stars, are introduced in Section II B. The radiation feedback and our approximate radiative transfer method are presented in Section II D. The scalar turbulent metal mixing model is described in Section II E. The non-equilibrium chemical network and the implementation of radiative cooling are detailed in Section II F. The mesh construction and refinement strategy is described in Section II G. Finally, the specific simulation setup for this work is presented in Section II H.

This framework is implemented in AREPO, an N -body and moving-mesh magnetohydrodynamical code [56–58]. Due to its quasi-Lagrangian nature, AREPO naturally provides adaptive resolution and maintains Galilean invariance for fluid dynamics.

A. Star formation

1. Pop III Star formation

The star formation criteria for the Pop III stars are based on the model implemented in Wise *et al.* [9] with modified density threshold. A gas cell is eligible to form a Pop III star particle if it satisfies the following conditions:

- The gas flow is convergent, i.e., $\nabla \cdot \mathbf{v}_{\text{gas}} < 0$;
- The gas number density n_{gas} exceeds a threshold n_{th} of $\max(1 \text{ cm}^{-3}, 0.5 n_{\text{Jeans}})$;
- The H_2 fraction of the gas is higher than 5×10^{-4} ;
- The metallicity of the gas is lower than $10^{-4} Z_{\odot}$,

where $n_{\text{Jeans}} \equiv \pi c_s^2 / (G \mu m_H (8 R_{\text{cell}})^2)$ is the numerical Jeans number density, and Z_{\odot} is solar metallicity. A density floor of 1 cm^{-3} is imposed to prevent spurious star formation in the low-density, low-temperature IGM. Such

a density criterion is similar to that adopted in THESAN-ZOOM [59], and is designed to be less sensitive to numerical resolution compared to the fixed density thresholds used in Wise *et al.* [9].. In particular, such a criterion effectively incorporates the condition of local gravitational instability, since the density threshold is evaluated relative to the resolved gas properties rather than being a fixed global value. Simulation tests show that the results are robust to variations in this value (see Appendix A). The density threshold is resolution-dependent to ensure that star formation converges across different resolution levels.

The criterion for the H_2 fraction is based on Tegmark *et al.* [60], ensuring that the gas can cool efficiently via molecular transitions within a Hubble time. The metallicity criterion is set to $10^{-4} Z_\odot$, motivated by early studies on the fragmentation of star-forming clouds [61, 62]. While later studies suggested that the critical metallicity for fragmentation could drop to $10^{-5} - 10^{-6} Z_\odot$ if dust cooling is considered [63, 64], our current framework does not explicitly track dust evolution. Therefore, we choose a conservative limit of $10^{-4} Z_\odot$. The potential impact of this metallicity criterion will be investigated in future work.

Once a gas cell satisfies these conditions, the star formation rate (SFR) is calculated as:

$$SFR = \varepsilon_* \cdot m_{\text{Gas}} / \tau_{\text{ff}}, \quad (1)$$

where ε_* is the star formation efficiency (SFE) and $\tau_{\text{ff}} \equiv \sqrt{3\pi/(32G\rho)}$ is the free-fall timescale of the gas.

The local SFE within a gas cloud is physically regulated by feedback from protostellar outflows, radiation from massive stars, and supernovae. Observational and theoretical studies of metal-enriched star formation indicate that these processes typically limit the SFE to a few percent up to $\sim 10\%$ [e.g., 65, 66]. Theoretical works further suggest that Pop III star formation is similarly self-regulated by radiative feedback [42, 43] and potentially magnetic outflows [67]. The resulting SFE depends on the interplay of these processes and the cloud properties. We performed comparison runs with $\varepsilon_* = 10\%$ and $\varepsilon_* = 1\%$. We found that reducing ε_* to 1% results in a moderate decrease in the total Pop III stellar mass (to $\sim 2/3$ of the fiducial value), indicating a sub-linear dependence on the local efficiency parameter. Meanwhile, the total mass of Pop II stars is also not significantly affected at $z = 10$ (see Appendix A). Using cloud-size high-resolution simulations, Jaura *et al.* [43] find that a cloud of $\sim 2700 M_\odot$ yields a total stellar mass of several tens to $\sim 100 M_\odot$, corresponding to an SFE of a few percent. For simplicity, we adopt a fixed fiducial value of $\varepsilon_* = 10\%$ for both Pop III and Pop II star formation.

Regarding the numerical implementation, we follow the stochastic approach of Springel and Hernquist [68]: a gas cell is converted into a star particle with a probability $p = 1 - \exp(-\varepsilon_* dt / \tau_{\text{ff}})$, where dt is the timestep of the gas cell. The mass of the newly formed star particle corresponds to the mass of the original gas cell. In our

fiducial high-resolution runs, the typical stellar particle mass is $\sim 100 - 200 M_\odot$. Given our adopted Pop III IMF with a mean mass of $\sim 28 M_\odot$ (see Sec. II A 2), each particle effectively represents a small multiple system of Pop III stars, whereas for Pop II stars, it represents a small stellar cluster. In cases where the star particle mass falls below $\sim 30 M_\odot$, the particle should still be interpreted as a statistical sampling unit of the IMF, rather than an individual physical star. No minimum stellar particle mass is imposed in the model, and the associated radiative and supernova feedback are injected according to IMF-averaged expectations in a stochastic sense.

2. The IMF of Pop III stars

The IMF of Pop III stars remains highly uncertain and is still a subject of active debate [3]. While early theories suggested that Pop III stars formed in isolation as extremely massive objects [e.g., 41], more recent high-resolution simulations indicate that the primordial accretion disk is likely to fragment, leading to a broader mass distribution [42, 43].

Since the primary aim of this paper is to introduce and evaluate our sub-grid framework for Pop III star formation and feedback, we adopt a representative and physically motivated IMF, rather than exploring the full parameter space of possible Pop III IMFs. Specifically, we use the fitting formula from Jaura *et al.* [43], which corresponds to a scenario where the star-forming region undergoes fragmentation. The fitting formula of the IMF is

$$\Phi(M) = \exp(-a(1/M)^b) M^{-c}, \quad (2)$$

where $\Phi(M) \equiv dN/dM$ represents the IMF, the fitting parameters are $a = 2.1419$, $b = 0.3920$, $c = 1.1670$. The IMF is normalized such that the integral over the mass range yields a unit mass. The lower and upper mass limits are set to $1 M_\odot$ and $100 M_\odot$, respectively. The IMF-weighted Pop III stellar mass is $\sim 28 M_\odot$. A comprehensive investigation into the impacts of different Pop III IMF slopes and mass limits will be presented in future work.

Regarding the numerical representation of stars, classic cosmological simulations typically assume that each star particle represents a Simple Stellar Population (SSP), as the mass resolution of these simulations is much higher than that of individual stars [69–71]. As computational power increases, the resolution of modern simulations can reach down to $\sim 1 M_\odot$, making it possible to perform galaxy or cosmological simulations that resolve individual stars [12, 72]. Such star-by-star simulations provide a more physically grounded description of stellar feedback compared to the IMF-weighted average approach used in SSP models. However, achieving the requisite mass resolution remains computationally prohibitive for large parameter space studies or massive systems. In this work, our star particles (typical median mass $\sim 100 - 200 M_\odot$)

represent small stellar clusters (or multiple stellar systems) sampled from the IMF. To bridge the gap between SSP treatments and single-star simulations, we implement a discrete feedback model. As described in Section II B, SN energy is released through stochastic Poisson sampling rather than continuous injection. This approach allows us to capture the stochastic nature of feedback—approximating the behavior of star-by-star simulations, while maintaining the computational efficiency of a subgrid framework suitable for lower resolutions.

3. Pop II star formation

Following the death of Pop III stars via core-collapse supernovae (CCSNe) or pair-instability supernovae (PISNe), metals are enriched into the surrounding environment. Subsequently, Pop II stars form in these metal-enriched regions. A gas cell is eligible to form a Pop II star particle if it meets the following criteria:

- The gas is convergent $\nabla \cdot v_{\text{Gas}} < 0$;
- The gas number density n_{Gas} exceeds a threshold n_{th} of $\max(10 \text{ cm}^{-3}, 0.5 n_{\text{Jeans}})$;
- The metallicity of the gas exceeds the critical threshold of $10^{-4} Z_{\odot}$;
- The gas temperature is lower than 10^3 K .

We adopt a higher density threshold 10 cm^{-3} compared to the Pop III case, reflecting the efficient cooling provided by metals, which allows the gas to collapse to higher densities before fragmentation. The calculation of the star formation rate (SFR) and the stochastic numerical implementation follow the same methodology as described for Pop III stars in Section II A 1.

In the simulation, each Pop II star particle represents a small stellar cluster following a Chabrier IMF [73]. The lower and upper stellar mass limits are set to $0.1 M_{\odot}$ and $40 M_{\odot}$, respectively.

B. Kinetic feedback from stars

In this work, we incorporate kinetic feedback mechanisms, including supernova (SN) explosions from both massive Pop III and Pop II stars, as well as stellar winds from massive Pop II stars. Due to their pristine composition (i.e., lack of metals), Pop III stars are not expected to experience the strong classical stellar winds characteristic of massive stars, which are driven by radiation pressure on metal spectral lines [74]. So we do not include stellar wind feedback for Pop III stars in our current framework.

1. Evolutionary track of Pop III stars

The evolutionary fate of Pop III stars is primarily determined by their initial stellar mass [e.g. 3, 17]. Based on current stellar evolution theories, the endpoints of Pop III stars can be categorized as follows:

- Stars with masses in the range $10 M_{\odot} \leq M_{\star} \leq 25 M_{\odot}$ end their lives as CCSNe, typically releasing a kinetic energy of $E_{\text{SN}} \sim 10^{51} \text{ erg}$.
- Stars in the range $25 M_{\odot} < M_{\star} \leq 40 M_{\odot}$ generally experience significant fallback, resulting in faint supernovae with explosion energies far below 10^{51} erg , or direct collapse into black holes.
- Stars with masses between $40 M_{\odot}$ and $\sim 140 M_{\odot}$ are expected to collapse into BHs, either directly or following mass loss via pulsational pair-instability (PPISN).
- Stars more massive than $260 M_{\odot}$ collapse directly into BHs as photodisintegration prevents the pair-instability explosion.

In this work, we adopt an upper mass limit of $100 M_{\odot}$ for the Pop III IMF, and therefore PISNe are not included. This choice is made to reduce the complexity of the feedback channels and to focus on the stability and convergence of the Pop III star formation model itself. We leave a more comprehensive treatment including PISNe for future work, with the variation of the IMF. We assign a canonical explosion energy of $E_{\text{SN}} = 10^{51} \text{ erg}$ to stars in the mass range $10 - 25 M_{\odot}$. For stars outside this range (i.e. $> 25 M_{\odot}$), we assume they collapse directly into black holes without releasing feedback energy. Although recent observations of metal-poor stars suggest possible chemical imprints of PISNe [e.g. 23], we reserve the investigation of PISN feedback and yields for future work.

2. SN feedback injection

Instead of releasing supernova energy instantaneously from a newly formed star particle, we account for the finite lifetimes of stars with different masses. The SN energy release rate, \dot{E}_{SN} , is calculated based on stellar evolution theory [75]:

$$\dot{E}_{\text{SN}} = \Phi(M_{\text{TO}}) \left| \frac{dM_{\text{TO}}}{dt} \right| E_{\text{SN}}, \quad (3)$$

where $\Phi(M)$ represents the IMF, and $M_{\text{TO}}(t_{\text{age}})$ is the main-sequence turn-off mass at the current age of the star particle t_{age} . The turn-off masses for Pop III stars are interpolated from the tables provided by Klessen and Glover [3], which rely on the stellar evolution models of Murphy *et al.* [40] and Ekström *et al.* [76]. For Pop III

CCSNe, we adopt a canonical explosion energy of $E_{\text{SN}} = 10^{51}$ erg.

Numerically, the SN energy release at each timestep dt in the simulation can be calculated by $\dot{E}_{\text{SN}}dt$. However, such an injection may make the energy injection lower than the energy released from one single SN event, especially when the mass resolution is high. To address this, we employ a stochastic injection method. At each timestep dt , the expected number of SN events, $\lambda = (\dot{E}_{\text{SN}} dt)/E_{\text{SN}}$, is calculated. We then determine the discrete number of SN events, N_{SN} , by sampling from a Poisson distribution with mean λ . The total energy injected in that timestep is then $E_{\text{inj}} = N_{\text{SN}}E_{\text{SN}}$. This ensures that energy is always injected in integer multiples of a single supernova event.

The coupling of feedback energy to the gas depends on whether the Sedov–Taylor phase of the supernova remnant (SNR) is resolved. We define two characteristic radii: the cooling radius R_{cool} [77], where radiative losses become significant, and the fade-away radius R_{fade} [78], where the SNR merges with the background medium. These are calculated as:

$$R_{\text{cool}} = 23.7 N_{\text{SN}}^{0.29} n^{-0.42} (Z/Z_{\odot} + 0.1)^{-0.5} \text{ pc}, \quad (4)$$

$$R_{\text{fade}} = 48.8 N_{\text{SN}}^{1/3} \left(\frac{n}{0.02 \text{ cm}^{-3}} \right)^{-1/3} \left(\frac{T}{10^7 \text{ K}} \right)^{-1/3} \text{ pc}, \quad (5)$$

where n , T and Z denote the number density, temperature, and metallicity of the gas cell hosting the star particle. We compare the cell radius, R_{cell} to the effective feedback radius $R_{\text{fb}} = \min(R_{\text{cool}}, R_{\text{fade}})$.

If $R_{\text{cell}} < R_{\text{fb}}$, the Sedov–Taylor phase is considered resolved. In this case, we inject the total feedback energy E_{inj} as thermal energy into the host gas cell.

If $R_{\text{cell}} > R_{\text{fb}}$, the Sedov–Taylor phase is unresolved, and the injection method depends on whether the cooling is efficient enough:

- **Case 1 ($R_{\text{cool}} < R_{\text{fade}}$):** The SNR cools radiatively before fading, entering the momentum-conserving phase. We therefore inject the terminal momentum, $p_{\text{terminal}} = \sqrt{2m_{\text{cool}}E_{\text{inj}}}$, distributed to the 32 nearest neighbors, where $m_{\text{cool}} = 4/3\pi\rho_{\text{cell}}R_{\text{cool}}^3$, and ρ_{cell} is the gas density of the host cell [79–81].
- **Case 2 ($R_{\text{cool}} > R_{\text{fade}}$):** The SNR merges with the background while still in the hot, adiabatic phase. In this regime, we inject 70% of E_{inj} as thermal energy into the host cell and 30% as kinetic energy into the 32 nearest neighbors, mimicking the energy partition of a Sedov–Taylor blast wave [77, 81, 82].

For Pop II stars, we similarly include CCSNe feedback for stars with masses $M_{\star} > 8 M_{\odot}$, utilizing the same numerical implementation as described above but adopting the standard Chabrier IMF [73].

3. Stellar winds from Pop II stars

We model the stellar winds from massive Pop II stars following the prescriptions of Vink *et al.* [83]. Although the original model explicitly depends on metallicity, $\dot{M} \sim (Z/Z_{\odot})^{0.85}$, in this work we adopt the mass-loss rates and velocities corresponding to solar metallicity as a simplified treatment since we find that the stellar wind is sub-dominant feedback channel. A more precise, metallicity-dependent treatment of stellar winds will be investigated in future studies. The adopted mass-loss rate, \dot{M}_{wind} , is given by:

$$\log_{10}(\dot{M}_{\text{wind}}) = \begin{cases} -6.688 + 2.21 \log(L_{\star}/10^5) \\ \quad -1.339 \log(M_{\star}/30) \\ \quad -1.601 \log(1.3/2.0) \\ \quad + 1.07 \log(T_{\text{eff}}/(2 \times 10^4)) \\ -6.697 + 2.194 \log(L_{\star}/10^5) \\ \quad -1.313 \log(M_{\star}/30) \\ \quad -1.226 \log(2.6/2.0) \\ \quad + 0.933 \log(T_{\text{eff}}/(4 \times 10^4)) \\ \quad -10.92[\log(T_{\text{eff}}/(4 \times 10^4))]^2 \end{cases}, \quad \text{if } T_{\text{eff}} < T_c \\ (6)$$

where the wind velocity, v_{wind} , is defined as:

$$v_{\text{wind}} = \begin{cases} 1.3v_{\text{esc}}, & \text{if } T_{\text{eff}} < T_c \\ 2.6v_{\text{esc}}, & \text{if } T_{\text{eff}} > T_c \end{cases} \quad (7)$$

Here, L_{\star} , M_{\star} , and T_{eff} denote the stellar luminosity, mass, and effective temperature in units of L_{\odot} , M_{\odot} and Kelvin, respectively. $v_{\text{esc}} \equiv \sqrt{2GM_{\star}/R_{\star}}$ is the escape velocity on the surface of stars, and $T_c = 25882$ K represents the critical temperature of the bi-stability jump.

For a single star particle representing a stellar population, the total wind momentum injection rate, \dot{P}_{sw} , is calculated by integrating over the surviving massive stars:

$$\dot{P}_{\text{sw}} = \int_{M_{\text{min}}}^{M_{\text{TO}}(t_{\text{age}})} \Phi(M) (\dot{M}_{\text{wind}}(M) v_{\text{wind}}(M)) dM, \quad (8)$$

where $\Phi(M)$ is the IMF and $M_{\text{TO}}(t_{\text{age}})$ is the main-sequence turn-off mass at the current age of the star particle. In the simulation, this momentum flux is injected spherically into the 32 nearest gas neighbors.

4. Dipole correction

The feedback energy or momentum from supernovae and stellar winds is distributed to surrounding gas cells according to their local volumes. However, a purely volume-weighted coupling cannot guarantee isotropy of

the injected fluxes. Anisotropic injection may bias the deposited momentum toward certain directions, leading to unphysical bipolar outflows. Hopkins *et al.* [84] demonstrated that such anisotropies can significantly distort galactic morphologies and even disrupt thin disks at high resolution. To alleviate this issue, they proposed a tensor renormalization scheme to enforce isotropy.

In this work, we adopt a simpler dipole correction to ensure that the injected feedback momentum has no net preferred direction. For the weights assigned to neighboring gas cells w_i , the correction enforces

$$\sum_i w_i = 1, \quad (9)$$

$$\sum_i w_i \mathbf{e}_i = \mathbf{0}, \quad (10)$$

where \mathbf{e}_i is the unit vector from the source star to the target gas cell. The initial (uncorrected) weights are defined as $w_i^{(0)} \equiv V_i / \sum_j V_j$, where V_i is the gas-cell volume. We then apply a minimal correction,

$$w_i = w_i^{(0)} (1 - \mathbf{e}_i \cdot \boldsymbol{\lambda}), \quad (11)$$

where the correction vector $\boldsymbol{\lambda}$ is obtained by solving the linear system

$$\mathbf{M} \cdot \boldsymbol{\lambda} = \mathbf{d}, \quad (12)$$

with $\mathbf{M} \equiv \sum_i w_i^{(0)} \mathbf{e}_i \mathbf{e}_i^T$ and $\mathbf{d} \equiv \sum_i w_i^{(0)} \mathbf{e}_i$. This system always has a unique solution as long as the local cell distribution spans three dimensions.

Although this correction guarantees momentum isotropy, it does not strictly ensure $w_i > 0$. In rare cases where negative weights appear (typically for highly anisotropic neighbor configurations), we clip the negative values to zero and renormalize the weights. This slightly relaxes the $\sum_i w_i \mathbf{e}_i = \mathbf{0}$ constraint, but the residual dipole is negligible in practice. Compared to the full tensor renormalization of [84], our approach is simpler to implement and sufficiently accurate for supernova feedback modeling, leaving only a minor quadrupole residual.

C. Mass return and metal yields

Stars will lose most of their mass from zero-age main-sequence star (ZAMS) to the end of their life through stellar wind on main sequence, the post-main-sequence evolution, or outburst at the end of their life. However, the certain fraction in different period depends on the metallicity and stellar mass. To maintain feasibility, we adopt a simplified model where the total mass loss is returned to the interstellar medium (ISM) in a single instantaneous event at the end of the life of the stars. This approach, while simplifying the precise timing, captures the crucial feedback of the total mass and metals returned. We argue that any uncertainties introduced by

this timing approximation are likely subdominant to the larger, more fundamental uncertainties inherent in modeling the early universe, such as the unknown IMF of Pop III stars.

Adopting treatment from some previous works [85, 86], the mass return rate from a stellar population is calculated as:

$$\dot{M}_{\text{return}} = \Phi(M_{\text{TO}}) \left| \frac{dM_{\text{TO}}}{dt}(t_{\text{age}}) \right| \Delta M, \quad (13)$$

where $\Delta M \equiv M_{\text{ZAMS}} - M_{\text{rem}}$ is the mass difference between the mass at ZAMS and the remnant of the star with mass $M_{\text{TO}}(t_{\text{age}})$.

The metal yield rate is calculated using a similar formulation [87]:

$$\dot{M}_{\text{Z}} = \Phi(M_{\text{TO}}) \left| \frac{dM_{\text{TO}}}{dt}(t_{\text{age}}) \right| m_{\text{Z,yields}}, \quad (14)$$

where $m_{\text{Z,yields}}$ is the metal return during the evolution of the star. In this work, M_{rem} and $m_{\text{Z,yields}}$ is obtained from the Yields Table in Nomoto *et al.* [88]. The injection of the mass return and metal yields follows the method of SN injection described in Section II B.

D. Radiation feedback

Instead of implementing full RT, which is computationally expensive, we employ a hybrid approach combining a short-range approximation with a long-range optical-thin tree-based RT method. The long-range optical-thin tree-based RT method is based on Zhu and Springel [89], which is based on Kannan *et al.* [90]. This approach, while sacrificing some accuracy compared to full RT, is computationally efficient and shares similarities with the Locally Extincted Background Radiation in Optically Thin Networks (LEBRON) method [91].

We divide the stellar radiation into two bands: the Lyman-Werner (LW) band (11.2–13.6 eV) and the ionizing band (13.6–100 eV), to capture the effects of radiation on H₂ dissociation and photoionization of the primordial gas.

Since the IGM is largely transparent to LW radiation in the early Universe, we adopt an optically thin approximation for this band, following the methods described in Zhu and Springel [89]. The radiation flux from each star particle is calculated as $F = L/4\pi r^2$. To accelerate the computation, radiative information is propagated via the gravitational tree. For the photodissociation of H₂ by LW radiation, we implement the self-shielding factor f_{sh} from Wolcott-Green *et al.* [92]:

$$f_{\text{sh}} = \frac{0.965}{(1 + x/b_5)^{1.1}} + \frac{0.035}{(1 + x)^{0.5}} \exp \left[-8.5 \times 10^{-4} (1 + x)^{0.5} \right], \quad (15)$$

where $x = N_{\text{H}_2}/5 \times 10^{14} \text{ cm}^{-3}$, and $b_5 = b/10^5 \text{ cm s}^{-1}$, N_{H_2} is the column density of H_2 , b is the Doppler broadening parameter. The column density is calculated by the local approximation $n_{\text{H}_2} \cdot L_{\text{sob}}$, where L_{sob} is the Sobolev-like length defined as $\rho/|\nabla\rho|$ [93].

In contrast to LW radiation, the early Universe is not optically thin to ionizing radiation. Ionizing photons form a Strömgren region around sources, beyond which the radiation field decays rapidly. We therefore assume that ionizing radiation is confined to this region. To determine the size of the ionized region, we perform an iterative neighbour search starting from the radius of the host gas cell of the sources, doubling the search radius in each iteration until the recombination rate is larger than the source luminosity:

$$\sum_i V_i n_{\text{H}}^2 \alpha > Q, \quad (16)$$

where $\alpha \equiv 8.4 \times 10^{-11} T^{-0.5} (T/10^3)^{-0.2} (1 + (T/10^6)^{0.7})^{-1}$ is the recombination rate of hydrogen [94], n_{H} is the hydrogen number density, Q is total ionizing photon release rate from the stars, and . While computationally efficient, this method assumes spherical symmetry and ignores the anisotropy of the surrounding gas distribution.

Once the ionizing region is defined, we calculate the 1D column density $N_{\text{H}}(r)$ along the line of sight from the star. The local radiation flux is then given by $F = L/(4\pi r^2) \exp(-N_{\text{H}}\sigma)$, where σ is the SED-weighted ionization cross-section. Additionally, we account for the self-shielding of dense gas clumps within the ionized region. The shielded flux for cold clumps is calculated as $F_s = F \exp(-n_{\text{H}} L_{\text{Jeans}}\sigma)$, where n_{H} is local hydrogen number density, L_{Jeans} is the local Jeans length. More accurate models considering anisotropy will be explored in future work.

The Spectral Energy Distribution (SED) of Pop III stars is modeled as a blackbody spectrum. The effective temperatures are derived from the stellar evolution calculations of Klessen and Glover [3], which is based on Murphy *et al.* [40]. We find that the difference between this blackbody approximation and the detailed photon rates is less than 10%. For each star particle, we integrate the SED over the adopted IMF.

For Pop II stars, the SED follows the treatment of young stellar populations in Zhu and Springel [89], but we exclude the X-ray component (radiation from SN remnants and high-mass X-ray binaries). The SED is modeled using the Binary Population and Spectral Synthesis [BPASS v2.3, 95] models with solar metallicity at an age of 10 Myr, assumed to be unchanged with stellar age. In Zhu and Springel [89], an escape fraction is set to mimic the shielding effect of star forming region and focus on the radiation on galaxy and CGM properties. However, in this work, the ionizing radiation is hard to escape the Stromgren region and the approximate radiative transfer within the region is calculated. For this reason, we do

not include the escape fraction here.

To maintain computational feasibility, we adopt a simplified temporal model where the SED of a stellar population is assumed to be constant over its main feedback phase. The radiation from Pop III populations is assumed to last for the first $10^{7.3} \text{ yr}$, corresponding to the lifetimes of $10 M_{\odot}$ stars. The radiation from Pop II populations is assumed to last for the first $10^{7.5} \text{ yr}$, corresponding to the lifetime of an $8 M_{\odot}$ star at solar metallicity. Although this neglects detailed temporal evolution, it captures the time-averaged radiative feedback, which is the dominant effect for the cosmological scales and long-term evolution studied here.

E. Turbulent metal mixing

We include a subgrid model for the unresolved turbulent transport of metals in the interstellar and circumgalactic medium, following a Smagorinsky-type [96] large eddy simulation (LES) approach [e.g. 97, 98]. In this framework, the evolution of the metal mass fraction Z is governed by an advection-diffusion equation,

$$\frac{\partial \rho Z}{\partial t} + \nabla \cdot (\rho Z \mathbf{v} - \rho D \nabla Z) = 0, \quad (17)$$

where ρ and \mathbf{v} denote the gas density and velocity, and D is the effective turbulent diffusion coefficient. We adopt a Smagorinsky-like prescription for the diffusion coefficient,

$$D = C_{\text{diff}} (2R_{\text{cell}})^2 |S| \quad (18)$$

where R_{cell} is the radius of the local Voronoi cell, $|S|$ is the norm of the traceless shear tensor of the velocity field, and C_{diff} is a dimensionless coefficient. The shear tensor is defined as

$$S_{ij} = \frac{1}{2} \left(\frac{\partial v_i}{\partial x_j} + \frac{\partial v_j}{\partial x_i} \right) - \frac{1}{3} (\nabla \cdot \mathbf{v}) \delta_{ij} \quad (19)$$

and its norm is computed as

$$|S| = \sqrt{2S_{ij}S_{ij}}. \quad (20)$$

Numerically, the diffusion equation is solved in a conservative form using an SPH-like pairwise discretization between neighbouring gas cells. We adopt $C_{\text{diff}}=0.15$ as our fiducial value. We perform comparison simulations with and without this turbulent diffusion module, and find that the inclusion of turbulent metal mixing increases the volume filling fraction of metal-enriched gas by approximately a factor of two at $z = 10$. A systematic exploration of the dependence on the diffusion strength will be presented in future work.

F. Chemistry and Cooling

In the early Universe, the assumption of chemical equilibrium for primordial gas often breaks down as the relevant reaction timescales can be comparable to or longer

TABLE I. Summary of the simulations we performed, presented and analyzed in this paper. L is the box size. ϵ_{DM} and ϵ_{Gas} is the gravitational softening length of DM and gas. m_{DM} is the mass resolution of the mass.

Simulation	L [cMpc/ h]	Total number of particles	ϵ_{DM} [cpc]	ϵ_{Gas} [cpc]	m_{DM} [M_{\odot}]
IC0	1	2×256^3	100	17	6.38×10^3
IC1	1	2×256^3	100	17	6.38×10^3
IC2	1	2×256^3	100	17	6.38×10^3
HRes	1	2×448^3	100	17	1.88×10^3
LRes	1	2×128^3	100	17	5.09×10^4

than the dynamical timescales. Furthermore, molecular hydrogen H_2 acts as the primary coolant facilitating the formation of the first stars. We therefore employ a non-equilibrium chemical network for nine species: i.e., H^0 , H^+ , He^0 , He^+ , He^{++} , H_2 , H_2^+ , H^- , e^- . The network includes 26 collisional and photo-ionization processes, with reaction rates adopted from Abel *et al.* [36], Glover and Abel [38], Katz *et al.* [94]. The chemical network includes the formation and destruction of atomic hydrogen, atomic helium and molecular hydrogen. We list these chemical reactions in Appendix B. We do not include deuterium chemistry, which becomes the dominant cooling channel at temperature $T < 200$ K and is essential for resolving the formation of individual Pop III stars. However, since the resolution of our current simulations is insufficient to resolve the collapse of individual protostellar cores, and this work focuses on larger-scale feedback effects, we neglect deuterium which is only important for direct Pop III star formation simulation.

Following previous treatment in cosmological simulations [59, 69, 71] Λ_{prim} , metal cooling/heating Λ_Z , and the Compton cooling due to the cosmic microwave background (CMB) Λ_C :

$$\Lambda = \Lambda_{\text{prim}} + \Lambda_Z + \Lambda_C. \quad (21)$$

The cooling rates for atomic primordial processes are taken from Table 1 of Katz *et al.* [94], which includes collisional excitation, collisional ionization, recombination, dielectric recombination, and free-free emission. For molecular cooling, we adopt the rates from Table 8 of [38], which assumes a fixed 3:1 ortho-to-para ratio for H_2 . This includes collisional cooling via the collision between H_2 and H^0 , H_2 , He^0 , H^+ , and e^- . We impose a temperature floor of 100 K for the cooling rates, as the neglect of deuterium chemistry renders the cooling function inaccurate below this threshold.

The heating rate due to photoionization and photodissociation is calculated as:

$$\varepsilon_i = \int_{\nu_T}^{\infty} \frac{4\pi J_{\nu}}{h\nu} \sigma_{\nu} (h\nu - h\nu_T) d\nu \text{ erg s}^{-1}, \quad (22)$$

where i represent different processes, and J_{ν} is the intensity of the radiation field obtained by the method mentioned in Section II D, ν_T is the threshold frequency for the relevant process.

We compute metal cooling/heating rates using CLOUDY [99] assuming chemical equilibrium. We generate a cooling/heating table, stored as HDF5 files.

The table stores the metal cooling/heating rate $\Lambda_Z = \Lambda_Z(n_H, T, Z, J_{\text{Pop III}}, J_{\text{Pop II}})$ that affected by stellar radiation, where $J_{\text{Pop III}}$ and $J_{\text{Pop II}}$ represent the intensity of stellar radiation from Pop III stellar population and Pop II stellar population.

The Compton cooling/heating rate due to CMB follows the previous works [94], which can be expressed as

$$\Lambda_C = 5.41 \times 10^{-36} n_e T (1+z)^4 \text{ erg s}^{-1} \text{ cm}^{-3}. \quad (23)$$

G. Adaptive refinement strategy

We adopt a Jeans-length based refinement criterion to ensure that the local Jeans scale is always resolved by at least four resolution elements (i.e. $N_J \geq 4$), preventing artificial fragmentation in dense regions [45, 59, 103]. To avoid excessive refinement in very dense and cold regions, which would otherwise drive the cell size to extremely small values and significantly increase the computational cost, we set a temperature floor T whenever the cell diameter falls below 4 pc. This floor does not affect the thermodynamics of already resolved gas, but simply prevents unlimited mesh refinement at high densities.

For de-refinement, we prevent merging of cells across strong gradients in density, temperature, velocity, or pressure. The tolerance factor is set to $f_{\text{gentle}} = 1.2$, meaning that a cell is excluded from de-refinement if its local physical quantities differ from the neighboring minimum or maximum by more than 20%. We further disable this gentle de-refinement criterion in two specific regimes:

- **Cold gas** $T < 3 \times 10^4$ K and $M_{\text{gas}} < 100 M_{\odot}$: We disable the gentle de-refinement constraint. This allows turbulent cold gas clouds to merge more aggressively. Since we do not aim to resolve the internal collapse of individual cold clumps below the Jeans floor, this reduces computational cost while maintaining consistency with our subgrid star-formation model (where the median gas mass is $\sim 100 - 200 M_{\odot}$);
- **Hot gas** $T > 3 \times 10^4$ K and $M_{\text{gas}} < 10 M_{\odot}$: We strictly prevent de-refinement for these gas cells. This ensures that the hot, supernova-driven outflow phase, which typically consists of low-mass, high-temperature cells, retains high mass resolution. This is crucial for accurately capturing the development and propagation of galactic outflows.

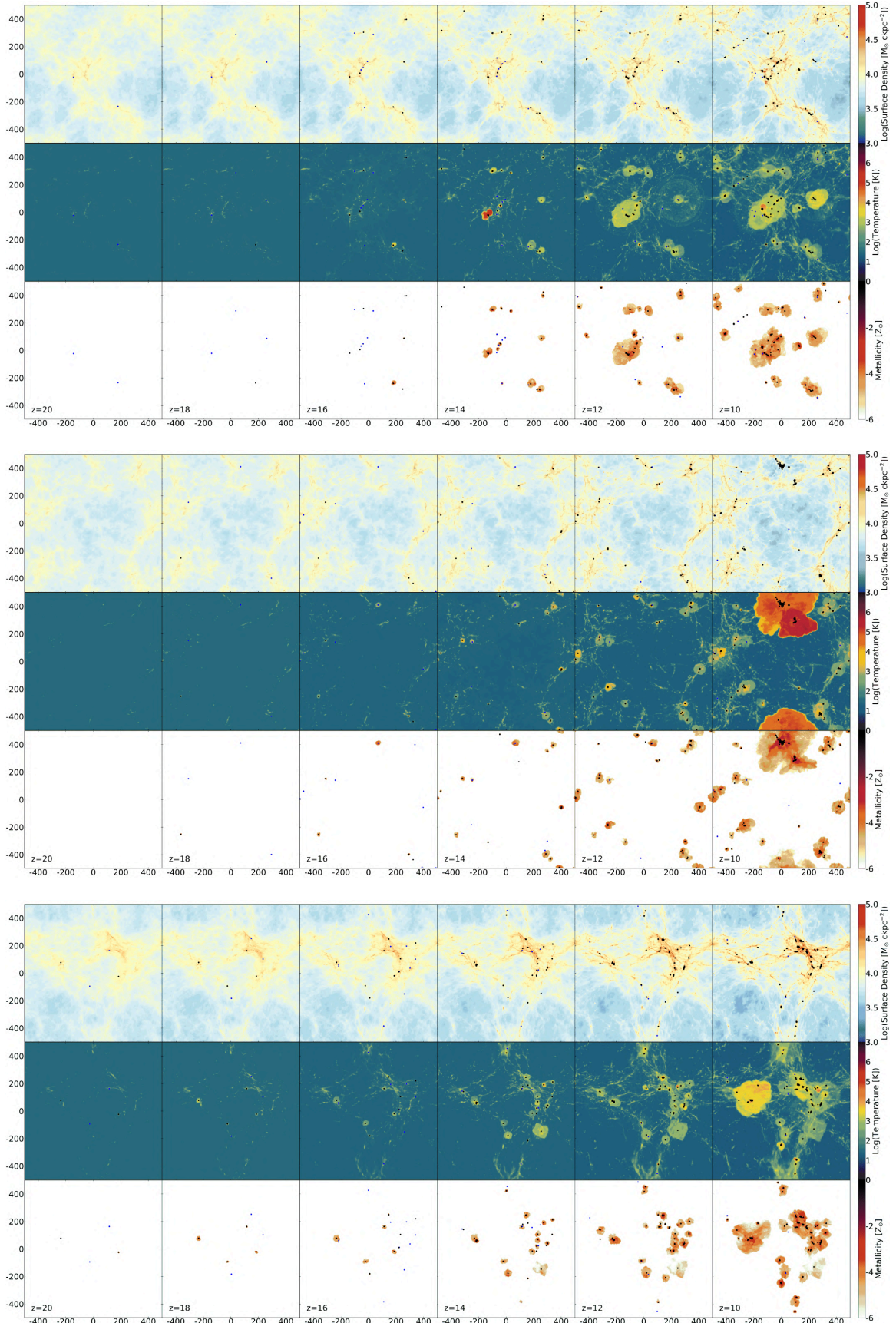


FIG. 1. The gas surface density, mass-weighted temperature, and metallicity distribution in the simulations with different initial conditions from $z = 20$ to $z = 10$. From the top to the bottom is IC0 (upper), IC1 (middle), and IC2 (bottom). The blue points represent the Pop III star while the black points represent the Pop II star. The first Pop III star forms at $z = 20 - 18$ in these three simulations.

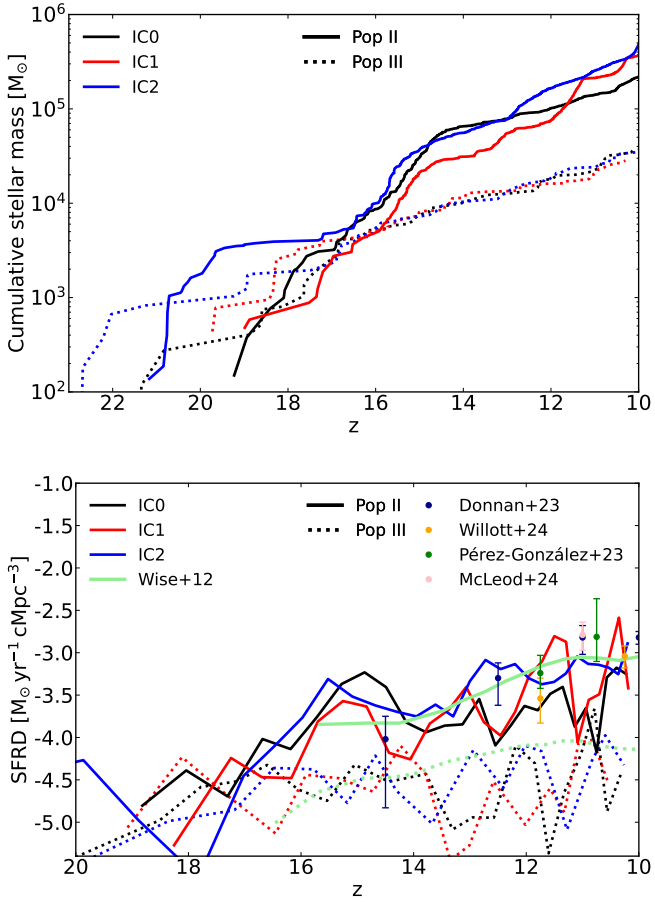


FIG. 2. *Upper*: The cumulative Pop III and Pop II stars in three simulations. The solid lines represent the Pop II star while the dashed lines represent the Pop III star. *Bottom*: The Pop III and Pop II star formation rate density (SFRD) from $z = 20$ to $z = 10$ in three simulations. The points (dark blue: Donnan *et al.* [28], orange: Willott *et al.* [100], green: Pérez-González *et al.* [101], pink: McLeod *et al.* [102]) represent the SFRD derive from the observed UV luminosity function. The green solid and dashed lines represent the simulations results about Pop II and Pop III SFRD in Wise *et al.* [9].

We tested the de-refinement criterion for these two specific regimes and obtain a convergent result with maximum computational efficiency.

H. Simulation setup

In this work, we perform a suite of cosmological hydrodynamical simulations in a periodic box with a comoving side length of $1 \text{ cMpc}/h$, evolving from $z = 127$ to $z = 10$.

Initial conditions are generated using the N-GENIC code [104, 105]. The adopted cosmology follows the *Planck* intermediate results [106], consistent with TNG: $\Omega_\Lambda = 0.6911$, $\Omega_m = 0.3089$, $h = 0.6774$, $\Omega_b = 0.0486$, $n_s = 0.9667$, and $\sigma_8 = 0.8159$. The initial power spec-

trum is computed using the Eisenstein and Hu [107] transfer function. The default resolution employs 256^3 dark matter particles and an equal number of gas cells in a $1 \text{ Mpc}/h$ periodic box, corresponding to mass resolutions of $\sim 1075 \text{ M}_\odot$ for gas and $\sim 6000 \text{ M}_\odot$ for dark matter. However, since we include the gas cell refinement, the highest gas cell resolution will change during the simulation and can reach $\sim 10 \text{ M}_\odot$. The gravitational softening length is 100 comoving pc for dark matter, while for gas cells and star particles, it is adaptive with a minimum of 17 comoving pc.

In addition to the fiducial run, we perform two simulations with different random realizations of the initial conditions, as well as two resolution tests with particle masses of 3 and $1/8$ times the fiducial runs. The main simulation parameters are summarized in Table I.

III. RESULTS

In this section, we present the global results from three simulations performed with different ICs but identical physical parameters and resolution. The time evolution of spatial distributions of gas density, temperature, and metallicity is presented in Section III A. The global star formation rate density (SFRD), together with a comparison to Wise *et al.* [9] and recent JWST observations, is shown in Section III B. Finally, in Section III C, we analyse the gas phase properties and the metal enrichment of the IGM driven by SN feedback.

A. Time evolution of gas structure and metal enrichment

Figure 1 displays the time evolution of gas surface density, mass-weighted temperature, and metallicity in the three simulations (IC0, IC1, and IC2) from $z = 20$ to $z = 10$. The sequence of snapshots illustrates the formation of large-scale structures and the subsequent star formation history.

In the IC0 and IC2 runs, dense structures form early, with the first Pop III stars already present at $z = 20$. In the IC0 simulation, only two Pop III stars have formed by this epoch. However, due to the stochastic sampling of SN feedback described in Section II B, these specific stars fall into mass ranges associated with direct collapse into black holes (or faint supernovae), resulting in no metal enrichment of the surrounding gas. In contrast, in the IC2 run, the Pop III stars fall into mass ranges associated with core-collapse supernovae, leading to metal enrichment of their surrounding gas. Consequently, Pop II stars begin to form from the metal-enriched gas. In the IC1 simulation, structure formation occurs somewhat later, with the first star appearing between $z = 20$ and $z = 18$.

As dense structures continue to evolve, star formation proceeds continuously across the simulation volume. Su-

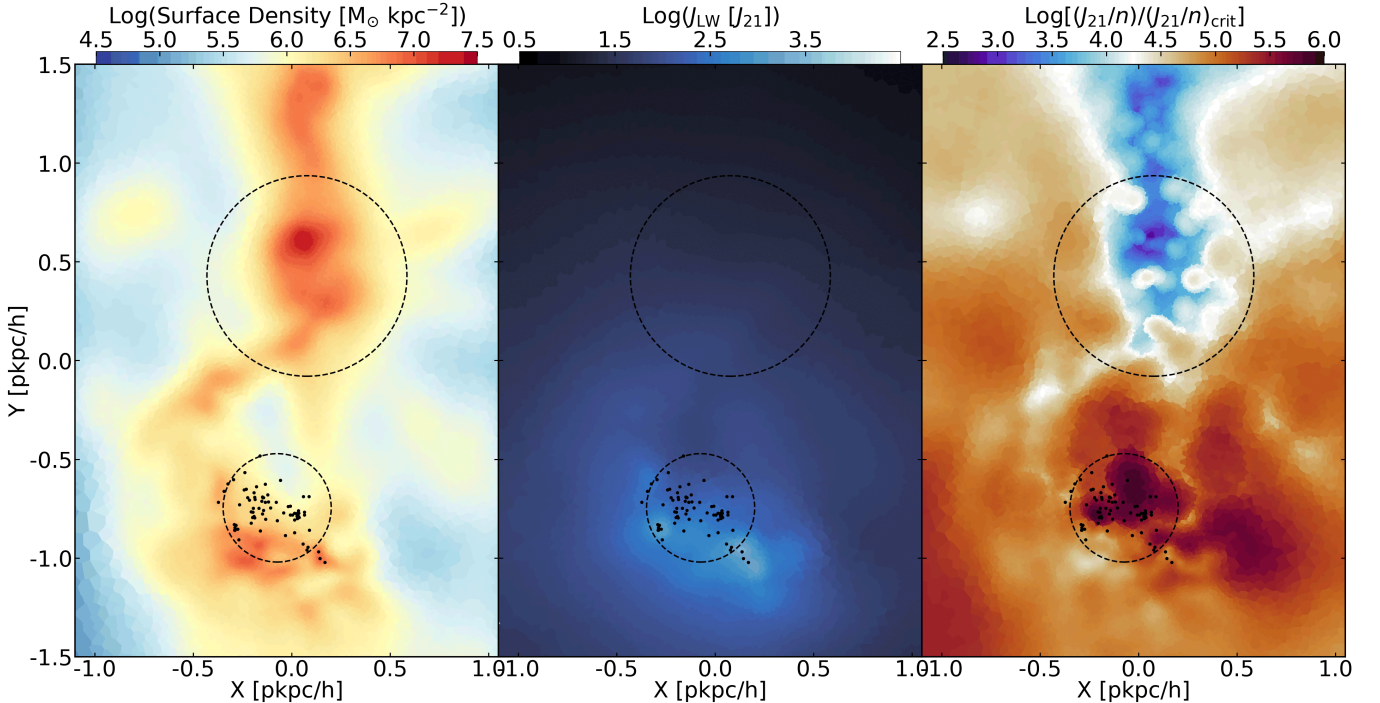


FIG. 3. The gas surface density, LW radiation intensity (J_{21}), and the ratio of the LW intensity to the critical threshold for H_2 cooling suppression for the two most massive subhalos in the IC0 simulation at $z = 10$. The black dashed circles represent the radius containing half of the total mass, and black points indicate star particles. The third panel displays $\log((J_{21}/n)/(J_{21}/n)_{\text{crit}})$; regions with values > 0 indicate where the LW background is strong enough relative to the density to dissociate H_2 and suppress cooling. This visualization explicitly confirms that the star-forming neighbor (bottom) generates a strong LW flux that irradiates the massive quiescent halo (top), preventing gas cooling and star formation in its center.

pernova explosions drive hot bubbles that expand and transport metals to larger scales. These metal-enriched regions grow and gradually connect to each other. By $z = 10$, the densest regions in all three simulations host a significant number of stars, driving large-scale, hot superbubbles. We discuss the detailed gas properties and metal enrichment processes in Section III C.

In the IC0 simulation, the imprint of ionizing radiation feedback is clearly visible in the $z = 12$ and $z = 10$ snapshots. At $(x, y) \sim (250, 100) \text{ ckpc}/h$, a slightly heated, spherical bubble with a radius of $\sim 100 \text{ ckpc}/h$ appears. This feature arises because the dense gas surrounding the source has been cleared, allowing ionizing photons to leak out from the small-scale region. The strictly spherical shape of this ionized bubble is an artifact of the one-dimensional approximation used for the column density calculation in our current radiation transport scheme; future work will incorporate more accurate angular-dependent column density calculations to capture anisotropic expansion.

B. Star formation

Having presented the qualitative evolution of gas properties in the previous section, we now turn to a quantita-

tive analysis of the stellar populations and star formation activity.

Figure 2 shows the time evolution of the cumulative stellar mass (upper panel) and star formation rate density (SFRD, bottom panel) for Pop III and Pop II stars across simulations with three different ICs. The upper panel demonstrates that all three ICs reproduce a similar total amount of Pop III and Pop II stars by the end of the simulations ($z = 10$). The total mass of Pop III stars is consistent across the runs, reaching around $3 \times 10^4 M_\odot$ at $z = 10$. For Pop II stars, the final stellar masses are generally around several $10^5 M_\odot$.

From the figure, we can see that the IC0 simulation produces approximately half the Pop II stellar mass of the other two simulations. Since Pop II stars preferentially form in massive halos, we investigate the gas state in the two most massive halos in the IC0 simulation. Figure 3 shows the distributions of surface density, LW radiation intensity, and the ratio of the LW intensity to the critical threshold required for H_2 cooling suppression for these two subhalos at $z = 10$. The black dashed lines represent the virial radii. The subhalo masses are $\sim 6 \times 10^7 M_\odot$ and $\sim 2.5 \times 10^7 M_\odot$ at $z = 10$. We find that these two massive subhalos reside in a dense filament (which is not fully shown in the figure) and are spatially close to each other, both belonging to the same large

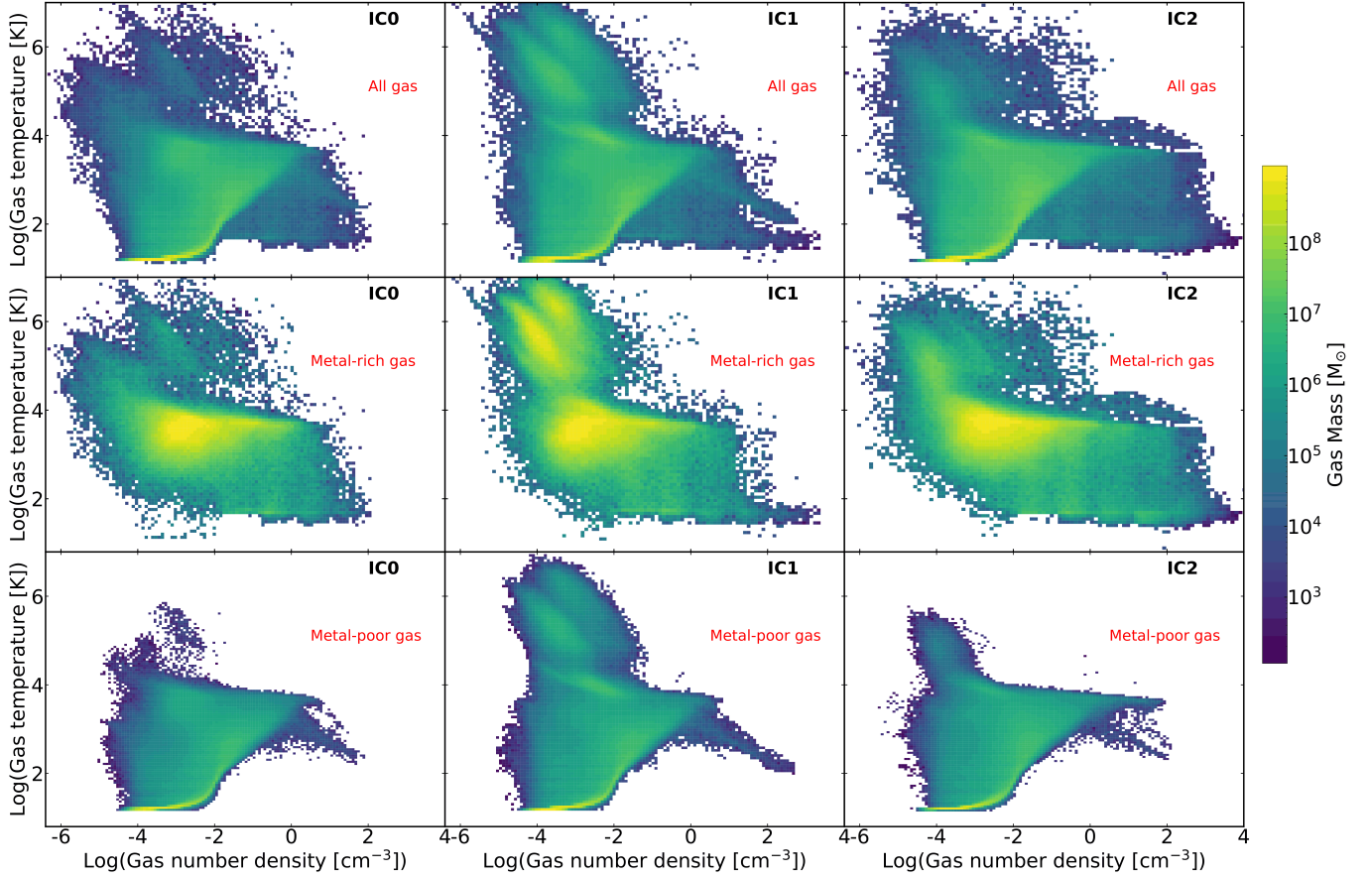


FIG. 4. The gas phase diagram of number density and temperature for all gas (upper), metal-poor gas (middle, defined by $Z/Z_{\odot} < 10^{-4}$) and metal-rich gas (bottom, defined by $Z/Z_{\odot} \geq 10^{-4}$) at $z=10$. Each row represents the results from the same simulation.

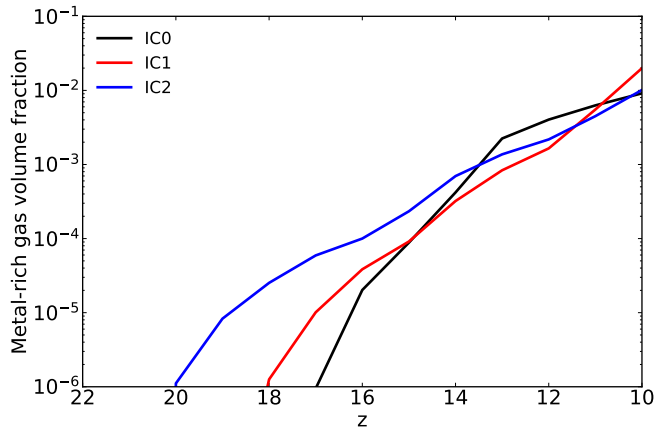


FIG. 5. The time evolution of the metal-rich gas ($Z/Z_{\odot} > 10^{-4}$) volume filling factor from $z = 20$ to $z = 10$.

friend-of-friend (FoF) halo. Furthermore, the most massive subhalo does not contain any stars, while the second most massive one exhibits significant star formation. As seen in the LW intensity map, continuous star formation in the secondary subhalo generates a strong LW back-

ground that irradiates its adjacent neighbor. The center of the most massive subhalo receives non-negligible LW irradiation, which suppresses H_2 formation and consequently prevents star formation in its center. To further quantify this effect, we compare the J_{21}/n with the critical threshold required to suppress H_2 cooling, adopting the criterion from Oh and Haiman [108]. As shown in the rightmost panel, the ratio of J_{21}/n to the critical value exceeds unity in the central region of the most massive subhalo. This confirms that the strong external irradiation dissociates H_2 efficiently, preventing the gas from cooling and collapsing into stars.

Since Pop II stars preferentially form in more massive halos compared to Pop III stars [e.g. 47], the suppression of star formation in the most massive subhalo of the IC0 simulation directly leads to the slightly lower total Pop II mass observed. In contrast, Pop III stars mainly form in minihalos, so their total amount is not affected significantly by this specific halo-halo interaction.

As shown in the bottom panel of Figure 2, for Pop III stars, after the first star forms, the SFRD increases and eventually plateaus at $\sim 10^{-4.5} M_{\odot} \text{ yr}^{-1} \text{ cMpc}^{-3}$ after $z \simeq 16$, although with significant stochastic variation. This value is close to that reported in Wise *et al.* [9], as

well as other Pop III cosmological simulations or semi-analytic models [e.g., 51, etc.]. The SFRD of Pop II stars increases with decreasing redshift. The values in the three simulations are similar to each other and consistent with Wise *et al.* [9], although the IC0 and IC1 simulations exhibit larger variations. Recent SFRD constraints inferred from observed UV luminosity functions [28, 100–102] are also presented in the figure. We see that the SFRD produced by our current model is consistent with these observations, indicating the validity of our framework.

C. Gas properties

Figure 4 presents the gas number density-gas temperature ($n - T$) phase diagrams for all gas, metal-poor gas, and metal-rich gas across three simulations with different ICs. We define metal-poor gas as gas with metallicity $Z < 10^{-4} Z_{\odot}$, and metal-rich gas as that with $Z \geq 10^{-4} Z_{\odot}$. The first row displays the total gas component. In all three simulations, the distribution exhibits a similar morphology, which can be categorized into three distinct phases: 1) hot diffuse gas ($n \lesssim 1 \text{ cm}^{-3}$, $T \gtrsim 10^4 \text{ K}$), generated by shock-heating from SN feedback; 2) cold diffuse gas ($n \gtrsim 10^{-2} \text{ cm}^{-3}$, $T \lesssim 10^4 \text{ K}$), corresponding to the IGM cooling adiabatically due to cosmic expansion; 3) cold dense gas ($n \gtrsim 1 \text{ cm}^{-3}$, $T \lesssim 10^4 \text{ K}$), which represents the primary fuel for star formation.

To disentangle the thermal properties of chemically distinct regions, we separately plot the metal-poor and metal-rich gas in the second and third rows of Figure 4. Comparing the metal-poor component with the total gas distribution reveals that metal-poor gas dominates the cold diffuse IGM phase. This is expected, as the large-scale IGM remains largely pristine, consistent with the metallicity maps shown in Figure 1. Notably, a population of hot, diffuse metal-poor gas is also present. This indicates that SN outflows sweep up and shock-heat the surrounding primordial gas, without immediately mixing metals into these swept-up shells. In the cold dense regime, the metal-poor gas follows a relatively tight sequence where temperature decreases with increasing density. This trend arises because cooling in this regime relies on molecular hydrogen (H_2); since the H_2 fraction correlates with gas density, the equilibrium temperature becomes density-dependent [e.g., 38]. We also identify a distinct branch of dense gas ($n > 1 \text{ cm}^{-3}$) with high temperatures ($\sim 10^4 \text{ K}$) in the IC2 simulation. We attribute this feature to strong local LW radiation fields from nearby star-forming regions, which dissociate H_2 and suppress cooling.

The third row of Figure 4 illustrates the properties of the metal-rich gas. Compared to the metal-poor component, metal-rich gas is preferentially found in the hot diffuse phase (filling the SN bubbles) rather than the cold diffuse IGM. In the cold dense regime, the metal-rich gas

exhibits a much broader scatter in the $n - T$ plane. This dispersion arises because metal-line cooling is highly efficient; gas can cool rapidly before it has time to collapse to higher densities, breaking the tight density-temperature correlation seen in primordial gas. The gas in the IC2 simulation extends to the highest densities, reflecting the deeper potential well of the most massive halo formed in that run. Overall, despite the varying IC, the thermodynamic properties of the gas phases are remarkably consistent across all three simulations.

Finally, we examine the time evolution of the metal-enriched gas volume fraction in Figure 5. Consistent with Figure 1, the IC2 simulation shows the earliest pollution, while IC0 is enriched later. However, at $z = 10$, the volume filling factor of metal-rich gas converges to a similar value of $\sim 1\%$ in all simulations. This suggests that, on cosmological scales, the signatures of the precise timing of the first Pop III supernovae are largely washed out at $z \sim 10$.

This filling factor is systematically higher than the value reported in previous cosmological simulations (e.g. $\sim 10^{-3}$ in Jaacks *et al.* 51). We attribute this difference primarily to the inclusion of an explicit turbulent metal mixing model in our simulations, which enhances the efficiency of metal transport.

IV. RESOLUTION DEPENDENCE

In this section, we investigate the numerical convergence and robustness of the subgrid model introduced in Section II by varying the simulation resolution. We adopt the IC0 simulation as our fiducial run and perform two additional runs with identical initial conditions but different mass resolutions: a high-resolution run (HRes) and a low-resolution run (LRes). The target gas mass resolution is $\sim 350 M_{\odot}$ in the HRes simulation and $\sim 4500 M_{\odot}$ in the LRes simulation, compared to $\sim 1000 M_{\odot}$ in the fiducial run. However, the minimum gas cell size is similar in all runs, as shown in the following results. We mainly present the impact of resolution on the star formation history. The resolution dependence of the gas phase properties in attached in Appendix C.

Figure 6 displays the time evolution of the cumulative stellar mass (top panel) and the star formation rate density (SFRD, bottom panel) for both Pop III and Pop II populations across simulations with varying resolutions. As shown in the top panel, the cumulative Pop III stellar mass is remarkably consistent between the HRes and IC0 simulations. The first Pop III stars in these high-resolution runs form at $z \sim 23$ and $z \sim 21$, respectively. In contrast, star formation in the LRes simulation is delayed, with the cumulative mass beginning to rise only at $z \sim 17$. Despite this initial discrepancy, the total cumulative stellar mass at $z = 10$ is similar among the three simulations, although the detailed timing of star formation remains strongly resolution-dependent. This result implies that the total reservoir of gas capable of collaps-

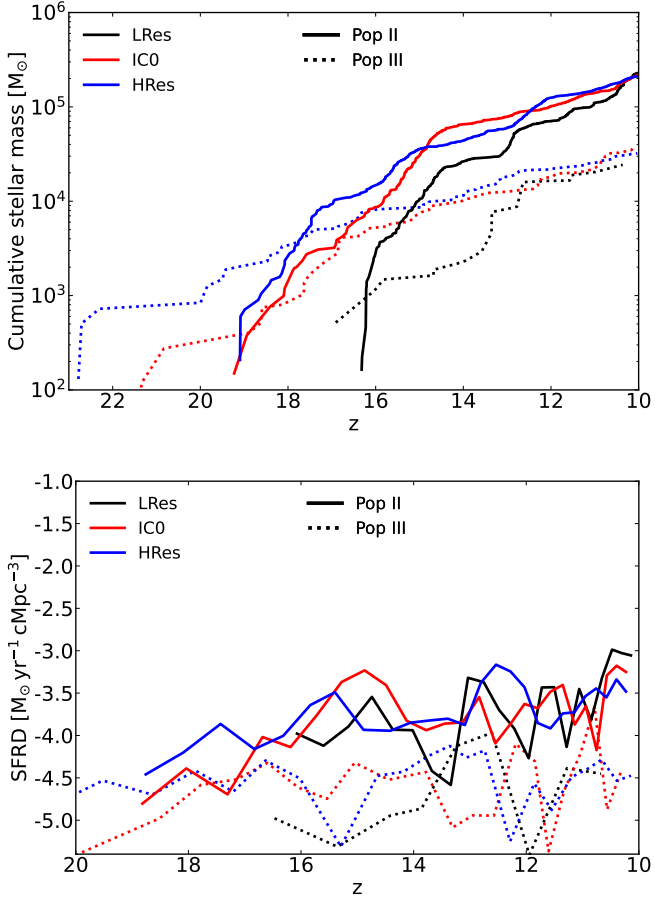


FIG. 6. *Upper*: The cumulative Pop III and Pop II stars in the simulations with IC0 but with different resolutions. *Bottom*: The Pop III and Pop II star formation rate density (SFRD) from $z = 20$ to $z = 10$ in three simulations.

ing and forming stars is relatively robust to resolution limits at $z = 10$, but the onset of structure formation is resolution-dependent.

For Pop II stars, we observe a similar trend. The evolution of the cumulative Pop II stellar mass shows even better agreement between the HRes and IC0 simulations compared to the LRes run. Furthermore, the resolution convergence appears to be faster for Pop II stars than for Pop III. Since Pop II formation is triggered by metal enrichment from prior Pop III supernovae, the delay in Pop III formation in the LRes run naturally leads to a delayed onset of Pop II stars ($z \sim 16$, compared to $z \sim 19$ in the high-resolution runs). Nevertheless, similar to the Pop III case, the total Pop II stellar mass at $z = 10$ is largely insensitive to resolution.

The bottom panel of Figure 6 shows the evolution of the SFRD. At $z > 16$, the SFRD is effectively zero in the LRes simulation due to the delayed onset of star formation. However, at $z < 14$, the SFRD in all simulations becomes comparable, exhibiting similar stochastic fluctuations. These results demonstrate that the IC0 and HRes simulations produce consistent star formation histories,

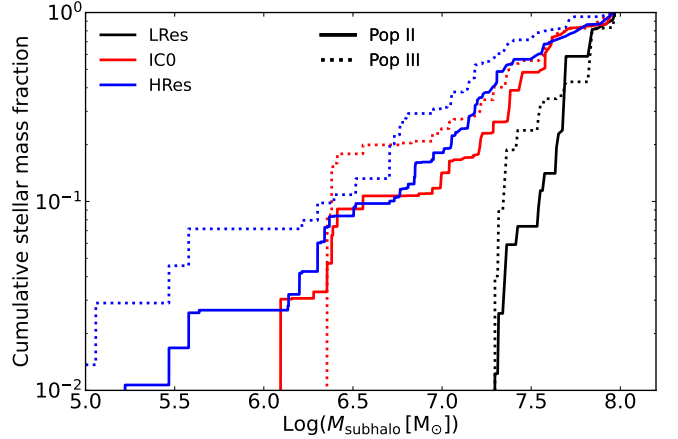


FIG. 7. The cumulative stellar mass fraction as a function of subhalo mass for simulations with three different resolutions (LRes, IC0 and HRes). Solid and dashed lines correspond to the contributions from Population II and Population III stars, respectively. The plot demonstrates that $\sim 90\%$ of stellar mass, for both Pop II and Pop III, is hosted by subhalos with mass $M_{\text{subhalo}} \gtrsim 10^{6.5} M_{\odot}$. All data are taken from the $z=10$ snapshot.

whereas the LRes simulation suffers from a systematic delay due to its inability to resolve the earliest minihalos. This indicates that our fiducial resolution (IC0) has achieved convergence for the physical quantities of interest in this work.

To better understand the origin of the discrepancy in the LRes simulation, we examine the cumulative distribution of Pop III and Pop II stellar mass as a function of host subhalo mass in Figure 7. In the HRes simulation, approximately 50% of both Pop III and Pop II stars reside in subhalos with $M_{\text{subhalo}} \lesssim 10^7 M_{\odot}$. Notably, only $\sim 10\%$ of the stellar mass is found in subhalos with $M_{\text{subhalo}} \lesssim 10^{6.5} M_{\odot}$. This implies that a simulation must resolve gas condensation within subhalos of mass $M_{\text{subhalo}} \sim 10^{6.5} M_{\odot}$ to capture the majority (90%) of the star formation history.

In the LRes simulation, the minimum mass of a star-hosting subhalo is $\sim 10^{7.3} M_{\odot}$. This indicates that the density threshold for Pop III star formation is only reached in halos above this mass limit, effectively missing the contribution from lower-mass minihalos capable of forming stars. Conversely, in the IC0 simulation, the minimum host mass is $\sim 10^{6.1} M_{\odot}$, sufficient to capture $> 90\%$ of the total star formation, explaining the strong agreement between the IC0 and HRes star formation histories. Interestingly, in the IC0 simulation, we observe that the minimum subhalo mass hosting Pop II stars is slightly lower than that of Pop III hosts. This implies that the metals triggering Pop II formation in these low-mass systems do not originate from in-situ Pop III supernovae within the same subhalo. Instead, they are likely enriched externally by supernovae in neighboring subhalos via inter-halo metal transport (external enrichment).

Furthermore, Pop II stars generally reside in more massive subhalos than Pop III stars. This trend is expected: Pop III stars predominantly form in low-mass minihalos with shallow potential wells, allowing supernova ejecta to escape efficiently (blow-away) without enriching the host halo. In contrast, massive subhalos can retain metals more effectively and are enriched via the accretion of metal-rich outflows from nearby minihalos or through the hierarchical merger of enriched progenitors.

V. SUMMARY

In this work, we presented a new Pop III + Pop II subgrid framework implemented in the moving-mesh code AREPO. The model includes (1) star-formation criteria for primordial and metal-enriched gas, (2) IMF-weighted stellar evolution with Poisson-sampled SN injection, which can mimic a quasi star-by-star behaviour, (3) stellar winds for massive Pop II stars, (4) approximate ionizing and LW radiation transport, (5) non-equilibrium primordial chemistry, (6) metal-line cooling tables coupled to stellar radiation, and (7) an adaptive, convergent Jeans-based refinement strategy. This combination of modules forms a self-consistent framework for Pop III + Pop II transition studies in cosmological volumes with AREPO code.

Using this framework, we performed multiple $1 \text{ cMpc}/h$ box simulations with different initial conditions and resolutions. Our main findings are:

- The model reproduces the UV-based Pop II star-formation-rate density inferred from recent JWST observations across all initial conditions, with only minor variations arising from local halo-halo interactions and LW irradiation (Figure 2 and 3).
- The volume filling factor of metal-enriched gas converges to $\sim 1\%$ at $z = 10$ across all resolutions, suggesting that our feedback model drives bubble expansion efficiently and robustly (5 and 12).
- Resolution tests show convergence once halos with mass $M_{\text{subhalo}} > 10^{6.5} M_{\odot}$ are resolved, indicating that capturing the dense gas in these systems is sufficient for converged Pop III/II star-formation histories. Under our model, this corresponds to 500–1000 DM particles for $M_{\text{subhalo}} \sim 10^{6.5} M_{\odot}$ subhalo (Figure 6 and 7).
- The total stellar mass formed by $z = 10$ is largely insensitive to IC and resolution, suggesting that early star formation is primarily regulated by the amount of gas able to collapse (Figure 2 and 6).

A key advantage of our framework is its computational efficiency. By employing an approximate RT scheme and a mesh refinement strategy, the model strikes a balance between physical fidelity and cost: a single $1 \text{ cMpc}/h$ fiducial run from $z = 127$ to $z = 10$ requires only $\sim 10^4$

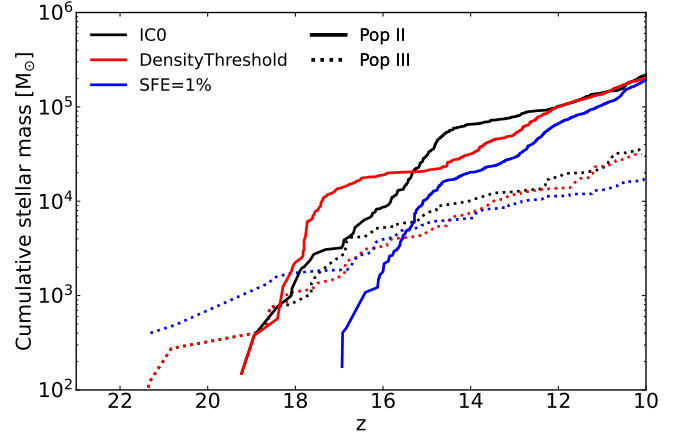


FIG. 8. The cumulative Pop III and Pop II stars in the simulation with the density threshold equal to $\max(10 \text{ cm}^{-3}, 0.5 n_{\text{Jeans}})$ and with SFE=1%.

CPU hours, typically using 640–896 MPI tasks on Intel Xeon Gold nodes. This tractable computational cost, significantly lower than full-RT calculations, enables the exploration of multiple initial conditions, rigorous convergence testing, and future large-scale parameter studies or zoom-in simulations.

Some simplifications remain in the current model. The current radiation model includes two bands (LW and ionizing), without explicit treatment of X-ray photons or spectral separation of H- and He-ionizing radiation. The ionizing region is also estimated using a spherical gas distribution around each source. Despite these approximations, the model successfully reproduces key global observables, indicating that the dominant physical processes are captured at the scales resolved here.

In future work, we will extend the radiation model and apply this framework to investigate Pop III IMF variations, X-ray feedback, and the environmental dependence of early metal enrichment.

ACKNOWLEDGMENTS

We thank Oliver Zier, Zhiyuan Yao, Zhi Li, Yizhou Liu, and Hang Yang for thorough comments, discussions and suggestions. We thank Volker Springel for kindly authorizing us the AREPO code. We acknowledge support from the National Natural Science Foundation of China (Grant No. 12588202) and the National Key Research and Development Program of China (Grant No. 2023YFB3002500). H.H. is supported by the NSFC Grant Nos. 12503012.

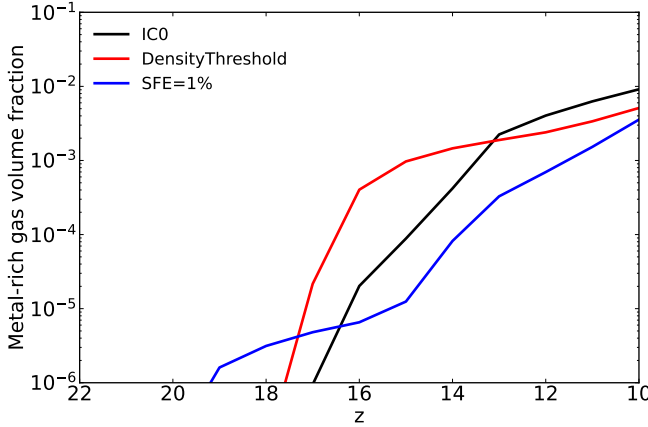


FIG. 9. The time evolution of the metal-rich gas ($Z/Z_{\odot} > 10^{-4}$) volume filling factor from $z = 20$ to $z = 10$.

Appendix A: Dependence on Star Formation Parameters

To assess the robustness of our results against the uncertainties in subgrid parameters, we performed two additional simulations based on the IC0 initial conditions. We varied the SFE to 1% and the star formation density threshold ($n_{\text{th}} = \max(10 \text{ cm}^{-3}, 0.5 n_{\text{Jeans}})$). Refer to Section II A 1 for details on the fiducial model.

Figure 8 presents the cumulative stellar mass evolution for these variations compared to the fiducial run (IC0). The simulation utilizing the alternative density threshold yields Pop III and Pop II star formation histories nearly identical to the fiducial run, indicating that our results are insensitive to variations in this criterion. Conversely, the SFE=1% model exhibits a noticeable delay in the onset of Pop II star formation, although the total stellar mass converges toward the fiducial result by $z = 10$. For Pop III stars, the total stellar mass in the low-SFE run is approximately 2/3 of that in the fiducial run. This suggests that the impact of the local SFE parameter on the global stellar mass is sub-linear.

Figure 9 illustrates the impact of these parameters on the volume fraction of metal-rich gas. Consistent with the stellar mass results, the time evolution of the volume filling factor in the density threshold simulation is roughly consistent with the fiducial run. However, the SFE=1% simulation displays a significant delay in metal enrichment. At $z = 10$, the volume filling factor in this run is approximately half that of the fiducial simulation. This reduction is likely a direct consequence of the suppressed Pop III star formation, which leads to fewer supernova events driving metal-enriched outflows.

Appendix B: Chemical network

The chemical network is selected from Abel *et al.* [36], Glover and Abel [38], Katz *et al.* [94], we

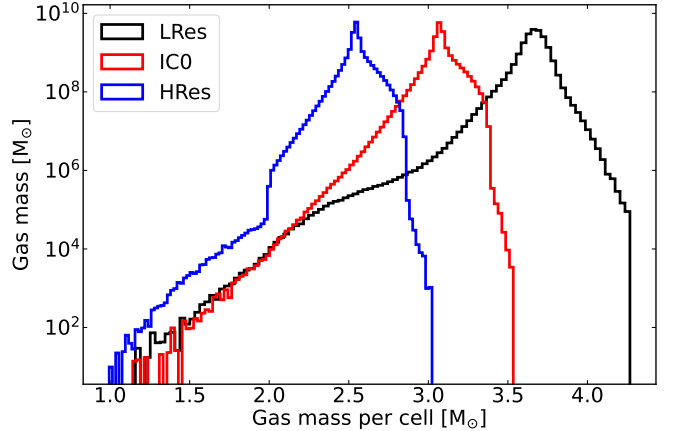


FIG. 10. The gas cell mass distribution in the simulations with IC0 initial condition but different resolutions.

choose some key atomic, molecular and photoionization/photodissociation processes. The full set of reactions is listed in Table II. The chemical network is solved by an in-house implementation of a backward Euler scheme combined with a Jacobian-Free Newton-Krylov method within Arepo.

Appendix C: Gas properties in the simulations with different resolutions

We examine the distribution of gas cell masses for the three simulations with different resolutions, as shown in Figure 10. The distribution exhibits a skewed shape with a tail extending towards low masses. The peak of the distribution corresponds to the target mass resolution of each simulation. The low-mass tail arises from Jeans refinement. Notably, the distribution of gas cells with mass $< 100 M_{\odot}$ is strikingly similar across all runs. In particular, in the HRes simulation, the total mass contained in these low-mass cells is effectively regulated. This behavior is a direct result of our refinement strategy described in Section II G, where we explicitly merge gas cells with mass $< 100 M_{\odot}$ if they are Jeans stable. The convergence of the gas mass distribution in the high-density regime explains why the three simulations produce similar total stellar masses, as previously shown in Figure 6.

We investigate the thermodynamic state of the gas in the three simulations. Figure 11 shows the $n-T$ phase diagrams for metal-poor and metal-rich gas separately. For the metal-poor gas, the LRes simulation lacks a stable, high-density, low-temperature branch due to insufficient resolution. Since the density criterion for Pop III star formation is set to $\min(0.5 n_{\text{Jeans}}, 1 \text{ cm}^{-3})$, the LRes simulation only marginally resolves the conditions for Pop III star formation. Comparing the HRes and IC0 simulations, we find that the cold dense gas is better resolved in the HRes run, with a larger reservoir of gas residing in the cold, dense phase. In addition, a distinct pop-

TABLE II. The chemical network for primordial gas used in this work. Reaction rates are taken from the references listed in the table.

Selected processes from Katz <i>et al.</i> [94]
$H + e^- \rightarrow H^+ + 2e^-$
$H^+ + e^- \rightarrow H + \gamma$
$He + e^- \rightarrow He^+ + 2e^-$
$He^+ + e^- \rightarrow He + \gamma$
$He^+ + e^- \rightarrow He^{++} + 2e^+$
$He^{++} + e^- \rightarrow He^+ + \gamma$
Selected processes from Abel <i>et al.</i> [36]
$H + e^- \rightarrow H^- + \gamma$
$H + H^- \rightarrow H_2 + e^-$
$H_2 + H^+ \rightarrow H_2^+ + H$
$H_2 + e^- \rightarrow 2H + e^-$
$H^- + e^- \rightarrow H + 2e^-$
$H^+ + H^- \rightarrow 2H$
Selected processes from Glover and Abel [38]
$H_2 + H \rightarrow 3H$
$H + H^+ \rightarrow H_2^+ + \gamma$
$H_2^+ + H \rightarrow H_2 + H^+$
$H + H \rightarrow H^+ + H + e^-$
$H^- + H \rightarrow 2H + e^-$
Selected photoionization/photodissociation processes from Abel <i>et al.</i> [36]
$H + \gamma \rightarrow H^+ + e^-$
$He + \gamma \rightarrow He^+ + e^-$
$He^+ + \gamma \rightarrow He^{++} + e^-$
$H^- + \gamma \rightarrow H + e^-$
$H_2 + \gamma \rightarrow H_2^+ + e^-$
$H_2^+ + \gamma \rightarrow H^+ + H$
$H_2^+ + \gamma \rightarrow 2H^+ + e^-$
$H_2 + \gamma \rightarrow H_2^* \rightarrow 2H$
$H_2 + \gamma \rightarrow 2H$

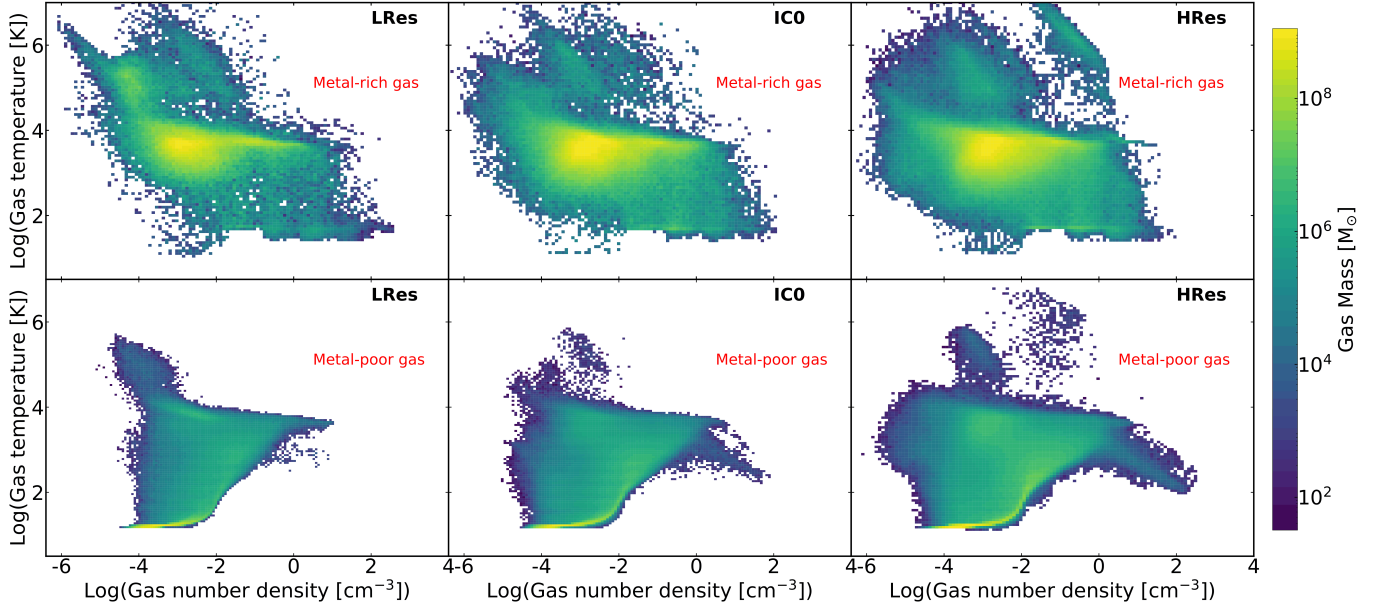


FIG. 11. Similar to Figure 4. The gas phase diagram of number density and temperature for metal-poor gas (upper, defined by $Z/Z_\odot < 10^{-4}$) and metal-rich gas (bottom, defined by $Z/Z_\odot \geq 10^{-4}$) at $z=10$. Each row represents the results from the same simulation.

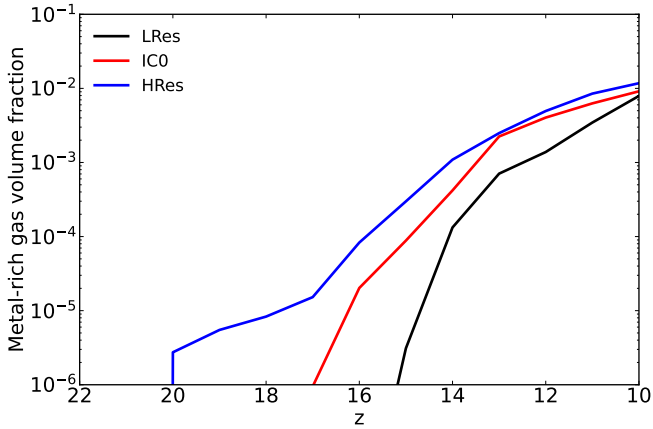


FIG. 12. Similar to Figure 5, but for the simulations with different resolution at $z = 10$.

ulation of gas with high temperature and high density ($T > 10^4$ K and $n \sim 10^{-2} - 1$ cm $^{-3}$) appears in the HRes simulation. This gas corresponds to the hot, shocked interiors of SN bubbles, which also appear in a previous simulation study [109]. Due to its higher resolution, the HRes simulation can better resolve the internal structure of these SN remnants compared to ICO.

The bottom panel of Figure 11 shows the phase diagram for metal-rich gas. In contrast to the metal-poor case, the LRes simulation successfully captures the dense, cold gas phase. Due to the effective cooling provided by metals, gas can undergo rapid collapse and cooling, allow-

ing the LRes simulation to better resolve the conditions required for Pop II star formation. We also observe a population of hot, dense, metal-enriched gas ($T > 10^4$ K and $n \sim 10^{-1} - 10^1$ cm $^{-3}$) in the HRes simulation, which again corresponds to the resolved interiors of metal-rich SN bubbles.

Figure 12 shows the time evolution of the metal-rich gas volume fraction across the three resolution levels. Similar to the star formation history, the onset of metal enrichment is delayed in the LRes simulation ($z \sim 15$) compared to the higher-resolution runs ($z \sim 20$) due to the delayed collapse of the first minihalos. However, a striking feature is the strong convergence at lower redshifts: at $z = 10$, the volume filling factor in all three simulations asymptotes to a nearly identical value of $\sim 1\%$. Since the volume filling factor is directly determined by the size of metal-enriched supernova bubbles, this convergence suggests that our feedback model drives bubble expansion robustly and efficiently across the resolutions considered.

In summary, while higher resolution naturally captures a broader and more detailed distribution of gas phases (particularly SN interiors), the simulation with our fiducial resolution (ICO) is sufficient to capture the key global star formation history. Conversely, the lower resolution (LRes) fails to capture the early star formation history, primarily because it cannot resolve the dense, primordial gas in minihalos at high redshifts. Therefore, our fiducial resolution represents an optimal balance between computational cost and the ability to resolve key physical processes.

[1] V. Bromm and R. B. Larson, The first stars, *Annu. Rev. Astron. Astrophys.* **42**, 79 (2004).

[2] V. Bromm, Formation of the first stars, *Rep. Prog. Phys.* **76**, 112901 (2013).

[3] R. S. Klessen and S. C. O. Glover, The first stars: Formation, properties, and impact, *Annu. Rev. Astron. Astrophys.* **61**, 65 (2023).

[4] R. Barkana and A. Loeb, In the beginning: the first sources of light and the reionization of the universe, *Phys. Rep.* **349**, 125 (2001).

[5] T. H. Greif, J. L. Johnson, V. Bromm, and R. S. Klessen, The first supernova explosions: Energetics, feedback, and chemical enrichment, *Astrophys. J.* **670**, 1 (2007).

[6] J. H. Wise and T. Abel, Resolving the formation of protogalaxies. iii. feedback from the first stars, *Astrophys. J.* **685**, 40 (2008).

[7] T. H. Greif, S. C. O. Glover, V. Bromm, and R. S. Klessen, The first galaxies: Chemical enrichment, mixing, and star formation, *Astrophys. J.* **716**, 510 (2010).

[8] J. S. Ritter, C. Safranek-Shrader, O. Gnat, M. Milosavljević, and V. Bromm, Confined population iii enrichment and the prospects for prompt second-generation star formation, *Astrophys. J.* **761**, 56 (2012).

[9] J. H. Wise, M. J. Turk, M. L. Norman, and T. Abel, The birth of a galaxy: Primordial metal enrichment and stellar populations, *Astrophys. J.* **745**, 50 (2012).

[10] M. Jeon, A. H. Pawlik, V. Bromm, and M. Milosavljević, Recovery from population iii supernova explosions and the onset of second-generation star formation, *Mon. Not. R. Astron. Soc.* **444**, 3288 (2014).

[11] G. Chiaki and J. H. Wise, Seeding the second star: enrichment from population iii, dust evolution, and cloud collapse, *Mon. Not. R. Astron. Soc.* **482**, 3933 (2019).

[12] K. Brauer, A. Emerick, J. Mead, A. P. Ji, J. H. Wise, *et al.*, Aeos: Star-by-star cosmological simulations of early chemical enrichment and galaxy formation, *Astrophys. J.* **980**, 41 (2025).

[13] A. Storck, H. Katz, J. Devriendt, A. Slyz, C. Cadiou, *et al.*, Megatron: The environments of population iii stars at cosmic dawn and their connection to present day galaxies, *arXiv e-prints*, arXiv:2510.06853 (2025).

[14] T. C. Beers and N. Christlieb, The discovery and analysis of very metal-poor stars in the galaxy, *Annu. Rev. Astron. Astrophys.* **43**, 531 (2005).

[15] A. Frebel and J. E. Norris, Near-field cosmology with extremely metal-poor stars, *Annu. Rev. Astron. Astrophys.* **53**, 631 (2015).

[16] V. Bromm and A. Loeb, High-redshift gamma-ray bursts from population iii progenitors, *Astrophys. J.* **642**, 382 (2006).

[17] A. Heger and S. E. Woosley, The nucleosynthetic signa-

ture of population iii, *Astrophys. J.* **567**, 532 (2002).

[18] T. Karlsson, V. Bromm, and J. Bland-Hawthorn, Pre-galactic metal enrichment: The chemical signatures of the first stars, *Rev. Mod. Phys.* **85**, 809 (2013).

[19] T. Hartwig, M. N. Ishigaki, C. Kobayashi, N. Tominaga, and K. Nomoto, Machine learning detects multiplicity of the first stars in stellar archaeology data, *Astrophys. J.* **946**, 20 (2023).

[20] S. Inoue, K. Omukai, and B. Ciardi, The radio to infrared emission of very high redshift gamma-ray bursts: probing early star formation through molecular and atomic absorption lines, *Mon. Not. R. Astron. Soc.* **380**, 1715 (2007).

[21] Q. Ma, U. Maio, B. Ciardi, and R. Salvaterra, Popiii signatures in the spectra of popii/i grbs, *Mon. Not. R. Astron. Soc.* **449**, 3006 (2015).

[22] W. Aoki, N. Tominaga, T. C. Beers, S. Honda, and Y. S. Lee, A chemical signature of first-generation very massive stars, *Science* **345**, 912 (2014).

[23] Q.-F. Xing, G. Zhao, Z.-W. Liu, A. Heger, Z.-W. Han, *et al.*, A metal-poor star with abundances from a pair-instability supernova, *Nature* **618**, 712 (2023).

[24] Á. Skúladóttir, S. Salvadori, A. M. Amarsi, E. Tolstoy, M. J. Irwin, *et al.*, Zero-metallicity hypernova uncovered by an ultra-metal-poor star in the sculptor dwarf spheroidal galaxy, *Astrophys. J. Lett.* **915**, L30 (2021).

[25] M. Castellano, A. Fontana, T. Treu, P. Santini, E. Merlin, *et al.*, Early results from glass-jwst. iii. galaxy candidates at $z = 9$ -15, *Astrophys. J. Lett.* **938**, L15 (2022).

[26] E. Curtis-Lake, S. Carniani, A. Cameron, S. Charlot, P. Jakobsen, *et al.*, Spectroscopic confirmation of four metal-poor galaxies at $z = 10.3$ -13.2, *Nat. Astron.* **7**, 622 (2023).

[27] B. E. Robertson, S. Tacchella, B. D. Johnson, K. Hainline, L. Whitler, *et al.*, Identification and properties of intense star-forming galaxies at redshifts $z \gtrsim 10$, *Nat. Astron.* **7**, 611 (2023).

[28] C. T. Donnan, D. J. McLeod, J. S. Dunlop, R. J. McLure, A. C. Carnall, R. Begley, *et al.*, The evolution of the galaxy uv luminosity function at redshifts $z = 8$ - 15 from deep jwst and ground-based near-infrared imaging, *Mon. Not. R. Astron. Soc.* **518**, 6011 (2023).

[29] R. Maiolino, H. Übler, M. Perna, J. Scholtz, F. D'Eugenio, *et al.*, Jades. possible population iii signatures at $z = 10.6$ in the halo of gn-z11, *Astron. Astrophys.* **687**, A67 (2024).

[30] E. Visbal, Z. Haiman, and G. L. Bryan, Limits on population iii star formation in minihaloes implied by planck, *Mon. Not. R. Astron. Soc.* **453**, 4456 (2015).

[31] R. H. Mebane, J. Mirocha, and S. R. Furlanetto, The persistence of population iii star formation, *Mon. Not. R. Astron. Soc.* **479**, 4544 (2018).

[32] A. Mesinger, S. Furlanetto, and R. Cen, 21cmfast: a fast, seminumerical simulation of the high-redshift 21-cm signal, *Mon. Not. R. Astron. Soc.* **411**, 955 (2011).

[33] H. Collaboration, Z. Abdurashidova, T. Adams, J. E. Aguirre, P. Alexander, *et al.*, Improved constraints on the 21 cm eor power spectrum and the x-ray heating of the igm with hera phase i observations, *Astrophys. J.* **945**, 124 (2023).

[34] S. Singh, N. T. Jishnu, R. Subrahmanyam, N. Udaya Shankar, B. S. Girish, *et al.*, On the detection of a cosmic dawn signal in the radio background, *Nat. Astron.* **6**, 607 (2022).

[35] S. Pochinda, T. Gessey-Jones, H. T. J. Bevins, A. Filalkov, S. Heimersheim, *et al.*, Constraining the properties of population iii galaxies with multiwavelength observations, *Mon. Not. R. Astron. Soc.* **531**, 1113 (2024).

[36] T. Abel, P. Anninos, Y. Zhang, and M. L. Norman, Modeling primordial gas in numerical cosmology, *New Astron.* **2**, 181 (1997).

[37] D. Galli and F. Palla, The chemistry of the early universe, *Astron. Astrophys.* **335**, 403 (1998).

[38] S. C. O. Glover and T. Abel, Uncertainties in h2 and hd chemistry and cooling and their role in early structure formation, *Mon. Not. R. Astron. Soc.* **388**, 1627 (2008).

[39] P. Marigo, L. Girardi, C. Chiosi, and P. R. Wood, Zero-metallicity stars. i. evolution at constant mass, *Astron. Astrophys.* **371**, 152 (2001).

[40] L. J. Murphy, J. H. Groh, S. Ekström, G. Meynet, C. Pezzotti, *et al.*, Grids of stellar models with rotation - v. models from 1.7 to 120 msun at zero metallicity, *Mon. Not. R. Astron. Soc.* **501**, 2745 (2021).

[41] S. Hirano, T. Hosokawa, N. Yoshida, H. Umeda, K. Omukai, *et al.*, One hundred first stars: Protostellar evolution and the final masses, *Astrophys. J.* **781**, 60 (2014).

[42] A. Stacy, V. Bromm, and A. T. Lee, Building up the population iii initial mass function from cosmological initial conditions, *Mon. Not. R. Astron. Soc.* **462**, 1307 (2016).

[43] O. Jaura, S. C. O. Glover, K. M. J. Wollenberg, R. S. Klessen, S. Geen, and L. Haemmerlé, Trapping of h ii regions in population iii star formation, *Mon. Not. R. Astron. Soc.* **512**, 116 (2022).

[44] V. Bromm and N. Yoshida, The first galaxies, *Annu. Rev. Astron. Astrophys.* **49**, 373 (2011).

[45] T. H. Greif, V. Springel, S. D. M. White, S. C. O. Glover, P. C. Clark, *et al.*, Simulations on a moving mesh: The clustered formation of population iii protostars, *Astrophys. J.* **737**, 75 (2011).

[46] L. Gao, N. Yoshida, T. Abel, C. S. Frenk, A. Jenkins, and V. Springel, The first generation of stars in the lambda cold dark matter cosmology, *Mon. Not. R. Astron. Soc.* **378**, 449 (2007).

[47] N. Yoshida, K. Omukai, and L. Hernquist, Protostar formation in the early universe, *Science* **321**, 669 (2008).

[48] A. Stacy, T. H. Greif, and V. Bromm, The first stars: mass growth under protostellar feedback, *Mon. Not. R. Astron. Soc.* **422**, 290 (2012).

[49] B. W. O'Shea, J. H. Wise, H. Xu, and M. L. Norman, Probing the ultraviolet luminosity function of the earliest galaxies with the renaissance simulations, *Astrophys. J. Lett.* **807**, L12 (2015).

[50] H. Xu, J. H. Wise, M. L. Norman, K. Ahn, and B. W. O'Shea, Galaxy properties and uv escape fractions during the epoch of reionization: Results from the renaissance simulations, *Astrophys. J.* **833**, 84 (2016).

[51] J. Jaacks, R. Thompson, S. L. Finkelstein, and V. Bromm, Baseline metal enrichment from population iii star formation in cosmological volume simulations, *Mon. Not. R. Astron. Soc.* **475**, 4396 (2018).

[52] B. Liu and V. Bromm, When did population iii star formation end?, *Mon. Not. R. Astron. Soc.* **497**, 2839 (2020).

[53] R. Sarmento and E. Scannapieco, The effects of radiative feedback and supernova-induced turbulence on

early galaxies, *Astrophys. J.* **935**, 174 (2022).

[54] H. Katz, M. P. Rey, C. Cadiou, O. Agertz, J. Blaizot, *et al.*, Megatron: Reproducing the diversity of high-redshift galaxy spectra with cosmological radiation hydrodynamics simulations, arXiv e-prints , arXiv:2510.05201 (2025).

[55] O. Zier, R. Kannan, A. Smith, E. Puchwein, M. Vogelsberger, *et al.*, The thesan-zoom project: Population iii star formation continues until the end of reionization, *Mon. Not. R. Astron. Soc.* **544**, 410 (2025).

[56] V. Springel, E pur si muove: Galilean-invariant cosmological hydrodynamical simulations on a moving mesh, *Mon. Not. R. Astron. Soc.* **401**, 791 (2010).

[57] R. Pakmor, V. Springel, A. Bauer, P. Mocz, D. J. Munoz, *et al.*, Improving the convergence properties of the moving-mesh code arepo, *Mon. Not. R. Astron. Soc.* **455**, 1134 (2016).

[58] R. Weinberger, V. Springel, and R. Pakmor, The arepo public code release, *Astrophys. J. Suppl.* **248**, 32 (2020).

[59] R. Kannan, E. Puchwein, A. Smith, J. Borrow, E. Garaldi, *et al.*, Introducing the thesan-zoom project: radiation-hydrodynamic simulations of high-redshift galaxies with a multi-phase interstellar medium, *The Open Journal of Astrophysics* **8**, 153 (2025).

[60] M. Tegmark, J. Silk, M. J. Rees, A. Blanchard, T. Abel, and F. Palla, How small were the first cosmological objects?, *Astrophys. J.* **474**, 1 (1997).

[61] V. Bromm, A. Ferrara, P. S. Coppi, and R. B. Larson, The fragmentation of pre-enriched primordial objects, *Mon. Not. R. Astron. Soc.* **328**, 969 (2001).

[62] R. Schneider, A. Ferrara, P. Natarajan, and K. Omukai, First stars, very massive black holes, and metals, *Astrophys. J.* **571**, 30 (2002).

[63] K. Omukai, T. Tsuribe, R. Schneider, and A. Ferrara, Thermal and fragmentation properties of star-forming clouds in low-metallicity environments, *Astrophys. J.* **626**, 627 (2005).

[64] R. Schneider, K. Omukai, A. K. Inoue, and A. Ferrara, Fragmentation of star-forming clouds enriched with the first dust, *Mon. Not. R. Astron. Soc.* **369**, 1437 (2006).

[65] R. C. Kennicutt and N. J. Evans, Star formation in the milky way and nearby galaxies, *Annu. Rev. Astron. Astrophys.* **50**, 531 (2012).

[66] M. Y. Grudić, D. Guszejnov, S. S. R. Offner, A. L. Rosen, A. N. Raju, *et al.*, The dynamics and outcome of star formation with jets, radiation, winds, and supernovae in concert, *Mon. Not. R. Astron. Soc.* **512**, 216 (2022).

[67] M. N. Machida, K. Omukai, T. Matsumoto, and S.-i. Inutsuka, The first jets in the universe: Protostellar jets from the first stars, *Astrophys. J. Lett.* **647**, L1 (2006).

[68] V. Springel and L. Hernquist, Cosmological smoothed particle hydrodynamics simulations: a hybrid multi-phase model for star formation, *Mon. Not. R. Astron. Soc.* **339**, 289 (2003).

[69] M. Vogelsberger, S. Genel, V. Springel, P. Torrey, D. Sijacki, *et al.*, Introducing the *Illustris* project: simulating the coevolution of dark and visible matter in the universe, *Mon. Not. R. Astron. Soc.* **444**, 1518 (2014).

[70] J. Schaye, R. A. Crain, R. G. Bower, M. Furlong, M. Schaller, *et al.*, The eagle project: simulating the evolution and assembly of galaxies and their environments, *Mon. Not. R. Astron. Soc.* **446**, 521 (2015).

[71] A. Pillepich, V. Springel, D. Nelson, S. Genel, J. Naiman, *et al.*, Simulating galaxy formation with the *IllustrisTNG* model, *Mon. Not. R. Astron. Soc.* **473**, 4077 (2018).

[72] Y. Deng, H. Li, B. Liu, R. Kannan, A. Smith, and G. L. Bryan, Rigel: Simulating dwarf galaxies at solar mass resolution with radiative transfer and feedback from individual massive stars, *Astron. Astrophys.* **691**, A231 (2024).

[73] G. Chabrier, Galactic stellar and substellar initial mass function, *Publ. Astron. Soc. Pac.* **115**, 763 (2003).

[74] J. I. Castor, D. C. Abbott, and R. I. Klein, Radiation-driven winds in of stars., *Astrophys. J.* **195**, 157 (1975).

[75] C. Maraston, Evolutionary population synthesis: models, analysis of the ingredients and application to high-z galaxies, *Mon. Not. R. Astron. Soc.* **362**, 799 (2005).

[76] S. Ekström, C. Georgy, P. Eggenberger, G. Meynet, N. Mowlavi, *et al.*, Grids of stellar models with rotation. i. models from 0.8 to 120 msun at solar metallicity (z = 0.014), *Astron. Astrophys.* **537**, A146 (2012).

[77] M. Li, J. P. Ostriker, R. Cen, G. L. Bryan, and T. Naab, Supernova feedback and the hot gas filling fraction of the interstellar medium, *Astrophys. J.* **814**, 4 (2015).

[78] M. Li, Y. Li, G. L. Bryan, E. C. Ostriker, and E. Quataert, The impact of type ia supernovae in quiescent galaxies. i. formation of the multiphase interstellar medium, *Astrophys. J.* **894**, 44 (2020).

[79] K. Thornton, M. Gaudlitz, H. T. Janka, and M. Steinmetz, Energy input and mass redistribution by supernovae in the interstellar medium, *Astrophys. J.* **500**, 95 (1998).

[80] T. Kimm and R. Cen, Escape fraction of ionizing photons during reionization: Effects due to supernova feedback and runaway ob stars, *Astrophys. J.* **788**, 121 (2014).

[81] A. Núñez, J. P. Ostriker, T. Naab, L. Oser, C.-Y. Hu, and E. Choi, Modeling for stellar feedback in galaxy formation simulations, *Astrophys. J.* **836**, 204 (2017).

[82] R. A. Chevalier, The evolution of supernova remnants. spherically symmetric models, *Astrophys. J.* **188**, 501 (1974).

[83] J. S. Vink, A. de Koter, and H. J. G. L. M. Lamers, Mass-loss predictions for o and b stars as a function of metallicity, *Astron. Astrophys.* **369**, 574 (2001).

[84] P. F. Hopkins, A. Wetzel, D. Kereš, C.-A. Faucher-Giguère, E. Quataert, *et al.*, How to model supernovae in simulations of star and galaxy formation, *Mon. Not. R. Astron. Soc.* **477**, 1578 (2018).

[85] G. S. Novak, J. P. Ostriker, and L. Ciotti, Feedback from central black holes in elliptical galaxies: Two-dimensional models compared to one-dimensional models, *Astrophys. J.* **737**, 26 (2011).

[86] F. Yuan, D. Yoon, Y.-P. Li, Z.-M. Gan, L. C. Ho, and F. Guo, Active galactic nucleus feedback in an elliptical galaxy with the most updated agn physics. i. low angular momentum case, *Astrophys. J.* **857**, 121 (2018).

[87] B. Zhu, F. Yuan, S. Ji, Y. Peng, L. C. Ho, *et al.*, Active galactic nuclei feedback in an elliptical galaxy (iii): the impacts and fate of cosmological inflow, *Mon. Not. R. Astron. Soc.* **524**, 5787 (2023).

[88] K. Nomoto, C. Kobayashi, and N. Tominaga, Nucleosynthesis in stars and the chemical enrichment of galaxies, *Annu. Rev. Astron. Astrophys.* **51**, 457 (2013).

[89] B. Zhu and V. Springel, The effect of local photoionization on the galaxy properties and the circumgalac-

tic medium in simulations of milky way-sized galaxies, *Mon. Not. R. Astron. Soc.* **533**, 4360 (2024).

[90] R. Kannan, G. S. Stinson, A. V. Macciò, J. F. Hennawi, R. Woods, *et al.*, Galaxy formation with local photoionization feedback - i. methods, *Mon. Not. R. Astron. Soc.* **437**, 2882 (2014).

[91] P. F. Hopkins, M. Y. Grudić, A. Wetzel, D. Kereš, C.-A. Faucher-Giguère, *et al.*, Radiative stellar feedback in galaxy formation: Methods and physics, *Mon. Not. R. Astron. Soc.* **491**, 3702 (2020).

[92] J. Wolcott-Green, Z. Haiman, and G. L. Bryan, Photodissociation of h₂ in protogalaxies: modelling self-shielding in three-dimensional simulations, *Mon. Not. R. Astron. Soc.* **418**, 838 (2011).

[93] N. Y. Gnedin, K. Tassis, and A. V. Kravtsov, Modeling molecular hydrogen and star formation in cosmological simulations, *Astrophys. J.* **697**, 55 (2009).

[94] N. Katz, D. H. Weinberg, and L. Hernquist, Cosmological simulations with treesph, *Astrophys. J. Suppl.* **105**, 19 (1996).

[95] J. J. Eldridge, E. R. Stanway, L. Xiao, L. A. S. McClelland, G. Taylor, *et al.*, Binary population and spectral synthesis version 2.1: Construction, observational verification, and new results, *Publ. Astron. Soc. Aust.* **34**, e058 (2017).

[96] J. Smagorinsky, General circulation experiments with the primitive equations, *Mon. Weather Rev.* **91**, 99 (1963).

[97] S. Shen, J. Wadsley, and G. Stinson, The enrichment of the intergalactic medium with adiabatic feedback - i. metal cooling and metal diffusion, *Mon. Not. R. Astron. Soc.* **407**, 1581 (2010).

[98] I. Escala, A. Wetzel, E. N. Kirby, P. F. Hopkins, X. Ma, *et al.*, Modelling chemical abundance distributions for dwarf galaxies in the local group: the impact of turbulent metal diffusion, *Mon. Not. R. Astron. Soc.* **474**, 2194 (2018).

[99] G. J. Ferland, M. Chatzikos, F. Guzmán, M. L. Lykins, P. A. M. van Hoof, *et al.*, The 2017 release cloudy, *Rev. Mex. Astron. Astrofis.* **53**, 385 (2017).

[100] C. J. Willott, G. Desprez, Y. Asada, G. T. E. Sarrouh, R. Abraham, *et al.*, A steep decline in the galaxy space density beyond redshift 9 in the canucs uv luminosity function, *Astrophys. J.* **966**, 74 (2024).

[101] P. G. Pérez-González, L. Costantin, D. Langeroodi, P. Rinaldi, *et al.*, Life beyond 30: Probing the -20 \pm 1 m uv \pm 17 luminosity function at 8 \pm 13 with the nircam parallel field of the miri deep survey, *Astrophys. J. Lett.* **951**, L1 (2023).

[102] D. J. McLeod, C. T. Donnan, R. J. McLure, J. S. Dunlop, D. Magee, R. Begley, *et al.*, The galaxy uv luminosity function at $z \approx 11$ from a suite of public jwst 1, 2, and cycle-1 programs, *Mon. Not. R. Astron. Soc.* **527**, 5004 (2024).

[103] J. K. Truelove, R. I. Klein, C. F. McKee, J. H. Holliman, II, L. H. Howell, and J. A. Greenough, The jeans condition: A new constraint on spatial resolution in simulations of isothermal self-gravitational hydrodynamics, *Astrophys. J. Lett.* **489**, L179 (1997).

[104] V. Springel, S. D. M. White, A. Jenkins, C. S. Frenk, N. Yoshida, *et al.*, Simulations of the formation, evolution and clustering of galaxies and quasars, *Nature* **435**, 629 (2005).

[105] R. E. Angulo, V. Springel, S. D. M. White, A. Jenkins, C. M. Baugh, and C. S. Frenk, Scaling relations for galaxy clusters in the millennium-xxl simulation, *Mon. Not. R. Astron. Soc.* **426**, 2046 (2012).

[106] P. Collaboration, P. A. R. Ade, N. Aghanim, M. Arnaud, M. Ashdown, *et al.*, Planck 2015 results. xiii. cosmological parameters, *Astron. Astrophys.* **594**, A13 (2016).

[107] D. J. Eisenstein and W. Hu, Power spectra for cold dark matter and its variants, *Astrophys. J.* **511**, 5 (1999).

[108] S. P. Oh and Z. Haiman, Second-generation objects in the universe: Radiative cooling and collapse of halos with virial temperatures above 10^4 k, *Astrophys. J.* **569**, 558 (2002).

[109] V. Bromm, N. Yoshida, and L. Hernquist, The first supernova explosions in the universe, *Astrophys. J. Lett.* **596**, L135 (2003).